ABSTRACT

Title of Dissertation: NONLINEAR DYNAMICS OF EXTENDED SYSTEMS: CHAOS FRONTS, RARE INTENSE EVENTS, AND GROWING NETWORKS

Jong-Won Kim, Doctor of Philosophy, 2002

Dissertation directed by: Professor Edward Ott
Department of Physics

We investigate the nonlinear dynamics of three extended systems: chaos fronts, rare intense events, and growing networks.

As the first example, we study the dynamics of the front separating a spatio-temporally chaotic region from a stable steady region using a simple model applicable to periodically forced systems. In particular, we investigate both the coarsening of the front induced by the inherent 'noise' of the chaotic region, and the long wavelength dynamics causing the front to develop cusps.

As the second example, we study the statistics and characteristics of rare intense events in two types of two dimensional Complex Ginzburg-Landau (CGL) equation based models. Our numerical simulations show finite amplitude collapse-like solutions which approach the infinite amplitude solutions of the nonlinear

Schrödinger (NLS) equation in an appropriate parameter regime. We also determine the probability distribution function (PDF) of the amplitude of the CGL solutions, which is found to be approximately described by a stretched exponential distribution, $P(|A|) \approx e^{-|A|^{\eta}}$, where $\eta < 1$. This non-Gaussian PDF is explained by the nonlinear characteristics of individual bursts combined with the statistics of bursts. Our results suggest a general picture in which an incoherent background of weakly interacting waves, occasionally, 'by chance', initiates intense, coherent, self-reinforcing, highly nonlinear events.

As the last example, we consider models for growing networks incorporating two effects not previously considered: (i) different species of nodes, with each species having different properties (such as different attachment probabilities to other node species); and (ii) when a new node is born, its number of links to old nodes is random with a given probability distribution. Our numerical simulations show good agreement with analytic solutions. As an application of our model, we investigate the movie-actor network with movies considered as nodes and actors as links.

NONLINEAR DYNAMICS OF EXTENDED SYSTEMS: CHAOS FRONTS, RARE INTENSE EVENTS, AND GROWING NETWORKS

by

Jong-Won Kim

Dissertation submitted to the Faculty of the Graduate School of the
University of Maryland, College Park in partial fulfillment
of the requirements for the degree of
Doctor of Philosophy
2002

Advisory Committee:

Professor Edward Ott, Chairman/Advisor
Dr. Parvez Guzdar
Professor Brian R. Hunt
Professor Wolfgang Losert
Professor Rajarshi Roy

ACKNOWLEDGEMENTS

I would like to express my gratitude to the people who have helped me carry out my graduate research and write this doctoral dissertation. In particular, I would like to thank my advisor Prof. Ott for his support, patience, and encouragement throughout my graduate studies. He has taught me innumerable lessons and insights on the academic research in general.

I am also very grateful to the members of my committee, Prof. Roy, Prof. Hunt, Prof. Losert, and Dr. Guzdar for comments and suggestions. Special thanks go to my collaborators, Prof. Venkataramani and Jay Vaishnav, who coauthored one of my research papers which become a part of this dissertation. I would like to thank my colleagues in the Chaos group for providing a good working atmosphere. I enjoyed many fruitful discussions with them during the tea time and the lunch seminar. I owe special thanks to my brother, sisters, and friends in Korea. They have given me much valuable advice and wisdom throughout my life. I also thank to my friends in the club, Korean Graduate Students Association, who share with me the excitement and difficulties of living in a foreign country.

Last, but not least, I would like to thank my parents. They have taught me how to live, love, and learn. Without their great love, I could not possibly have accomplished this. This dissertation is dedicated to them.

To all of you, thank you from the bottom of my heart.

TABLE OF CONTENTS

LIST OF FIGURES

Chapter 1

Introduction

In this dissertation we investigate the nonlinear dynamics of extended systems. Examples of extended systems occur in many real situations, three of which are studied in this dissertation: chaos fronts (Chapter 2), rare intense events (Chapter 3), and growing networks (Chapter 4). In the first two situations, we observe nontrivial collective behaviors in systems that are *spatially* extended (spatiotemporal chaotic patterns in Chapter 2 and "bursts" in Chapter 3). The third situation is representative of another type of extended system (Chapter 4), which might be designated *topologically extended,* which occurs when many units are connected to form a large network.

In Chapter 2 we study the dynamics of the front separating a spatiotemporally chaotic state from a stable steady ordered state. We construct a Continuum Coupled Map (CCM) model to incorporate the essential feature that both a stable steady homogeneous attractor and a spatiotemporally chaotic attractor exist. Using our CCM model, which has two stable competing patterns in the same parameter regime, we numerically investigate the coarsening of the front due to the inherent 'noise' associated with the spatiotemporal chaos and cusp formation induced by initial long wavelength perturbations of the front location from the flat

state.

In Chapter 3 we study the phenomena of rare intense events ("bursts") which is reported in many spatiotemporal dynamical systems. The characteristic feature of rare intense events is a non-Gaussian tail in the event size probability distribution function, which can result from strong nonlinearity of the events. The enhancement of the event size tail might be expected if large amplitudes are nonlinearly self-reinforcing. Such nonlinear self-reinforcements is present in the nonlinear Schrödinger (NLS) equation. In the limit of small dissipation/instability the complex Ginzburg-Landau (CGL) equation displays a solution similar to the NLS solution. Furthermore, over a sufficiently large spatial domain, these events occur intermittently in space and time. Thus, in this limit, the CGL equation may be considered as a model for the occurrence of rare intense events. The probability distribution function (PDF) of the amplitude of the solutions is observed to be non-Gaussian in our numerical experiments. This non-Gaussian PDF is explained by the nonlinear characteristics of individual bursts combined with the statistics of bursts. Our results lead us to the following picture for the occurrence of rare intense events in our system. Linear instability and nonlinear wave saturation lead to an incoherent background of small amplitude waves. This background is responsible for the observed Gaussian behavior of our probability distribution functions in the *small* amplitude region. When, by chance, the weakly interacting waves locally superpose to create conditions enabling nonlinear, coherent self-reinforce, a localized collapse-like event is initiated. Collapse takes over, promoting large, rapid growth and bursting of amplitude. This is followed by a burn-out phase in which the energy is rapidly dissipated due to the generation of small scale structure by the burst. We believe that elements of the above general picture may be

relevant to a variety of physical situations where rare intense events occur.

In Chapter 4 we study a growing network in which structual complexity originates from dynamical evolution of the network. The most common feature of growing networks is power law distributions (*e.g.,* the number of nodes with k links is observed to be $n_k \sim k^{-\nu}$, where ν is a scaling exponent). We attempt to construct general growing network models featuring two effects which have not been considered previously: multiple species of nodes and initial link distributions. As an application of our model, we investigate the movie-actor network with movies considered as nodes and actors as links (*i.e.*, if the same actor appears in two movies there is a link between the two movies). Moreover, we consider theatrical movies and made-for-television movies to constitute two different species. We believe that the effect of multiple species nodes and initial link probability may be important for modeling other complicated networks.

Chapter 2

Chaos Fronts

2.1 Preview

In this chapter we study the dynamics of the front separating a spatiotemporally chaotic state from a stable steady ordered state. Such situations occur in many experimental settings. In an experiment on a vertically vibrating granular monolayer of spheres [1] both a state at rest on the plate and a chaotically bouncing state are stable. When a small perturbation is applied to the stationary state, the chaotic state is observed to invade the stable state through a propagating front. In a Rayleigh-Bénard convection experiment [2] both straight rolls and spiral defect chaos are stable under some conditions and it is observed that a region of straight rolls is invaded by a region of spiral defect turbulence.

For our study we employ a type of model called a Continuum Coupled Map (CCM) introduced in Ref. [3]. Models of this type (Sec. 2.2) are appropriate to periodically forced systems (such as that in the experiment of the Ref. [1]). In common with other generic models, like the complex Ginzburg-Landau equation or the Swift-Hohenberg equation, CCM models are meant to incorporate the minimal basic properties capable of reproducing the phenomena of interest. With this in

mind we construct our CCM model to incorporate the essential feature that both a stable steady homogeneous attractor and a spatiotemporally chaotic attractor exist. Using our CCM model, we numerically investigate two phenomena: (i) the coarsening of the front due to the inherent 'noise' associated with the spatiotemporal chaos (Sec. 2.3), and (ii) cusp formation induced by initial long wavelength perturbations of the front location from the flat state (Sec. 2.4).

With respect to (i), an important concept used to study various coarsening processes is scaling. For a large number of systems (e.g., see Ref. [4]), it is found that the interface width due to roughening, $w(t)$, increases as a power of time, $w(t) \sim t^{\beta}$. The width eventually saturates at a value that increases as a power of the system size, $w(L_x) \sim L_x^{\alpha}$. These scaling properties are also observed in our model, and we determine and discuss the scaling exponents α and β that we find.

With respect to (ii), we argue that on long scale [i.e., long compared to $w(t)$], our fronts propagate at constant speed in a direction locally normal to the interface. We show that this basic property explains the mechanism of cusp formation and the evolution of the shape of the fronts observed in our numerical simulations.

2.2 CCM Model

As in reference [3], we consider a CCM model which maps a field $\xi_n(\vec{x})$ forward from time n to time $n+1$. With reference to a system driven periodically in time (e.g., as in [1]), we may think of $\xi_n(\vec{x})$, with $n = 1, 2, \cdots$, as being the system state stroboscopically sampled once each period. Furthermore, we consider $\vec{x} = (x, y)$ to be two-dimensional, and, for simplicity, we take ξ_n to be a scalar field. The CCM model mapping ξ_n to ξ_{n+1} consists of two steps: The first step is a nonlinear local operation in which a one-dimensional map M is applied to $\xi_n(\vec{x})$ at each point in

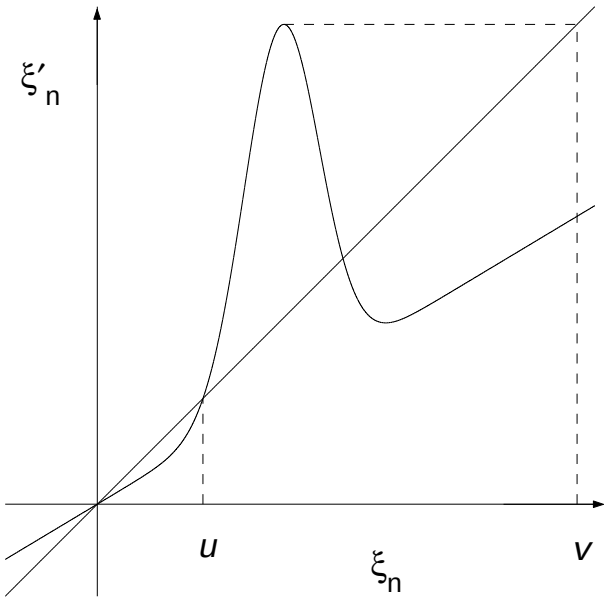

Figure 2.1: Schematic (not to scale) of the model map.

space,

$$\xi'_n(\vec{x}) = M(\xi_n(\vec{x})). \tag{2.1}$$

The second step is a translationally invariant linear operation coupling the dynamics at nearby spatial locations. The most general such coupling is conveniently expressed in terms of the spatial Fourier transform. If $\hat{\xi}_n(\vec{k})$ is the spatial Fourier transform of $\xi_n(\vec{x})$, then we write $\hat{\xi}_{n+1}(\vec{k})$ as

$$\hat{\xi}_{n+1}(\vec{k}) = \check{f}(\vec{k})\hat{\xi}'_n(\vec{k}), \tag{2.2}$$

from which $\xi_{n+1}(\vec{x})$ is obtained by inverse Fourier transforming.

The model is then specified by the choice of the nonlinear map M and the linear spatial coupling $\check{f}(\vec{k})$. We make these choices so as to include the minimum properties that we hypothesize are relevant for the investigated phenomena [5]. Since we desire the simultaneous existence of a stable steady state as well as a

spatiotemporally chaotic state, we choose the map M to have a stable fixed point attractor and a chaotic attractor. A convenient choice having this property is given by

$$M(\xi) = r\xi + A\exp[-(\xi-1)^2/\sigma^2] - A\exp(-1/\sigma^2). \tag{2.3}$$

Referring to Fig. 2.1, we see that this map has a stable fixed point at $\xi = 0$, for $r < 1$. Moreover, any initial point in $\xi < u$ is attracted to this point. We also see from Fig. 2.1 that the interval $u < \xi < v$ is mapped into itself. Thus there is (at least) one attractor in this interval. For the parameter values A, r, and w that we investigate ($A = 7.0, r = 0.4, \sigma = 0.29$) there is one attractor in $u < \xi < v$ and it is chaotic.

Our choice of the spatial coupling $\check{f}(\vec{k})$ is similarly motivated by a desire for simplicity. We assume that the coupling is isotropic. Thus we can write $\check{f}$ as $\check{f}(\vec{k}) = f(k)$, where $k = |\vec{k}|$. Taking $f(k) \geq 0$ we write

$$f(k) = \exp[\gamma(k)], \tag{2.4}$$

where $\gamma(k)$ is a wavenumber-dependent growth/damping rate per period. Since we want the spatiotemporal chaos to have a finite spatial correlation scale, such a scale must be reflected in our choice of $\gamma(k)$. Denoting this scale by k_0^{-1}, we make the following simple choice [3] for $\gamma(k)$,

$$\gamma(k) = \frac{1}{2}\left(\frac{k}{k_0}\right)^2\left[1 - \frac{1}{2}\left(\frac{k}{k_0}\right)^2\right]. \tag{2.5}$$

Thus $\gamma(k) > 0$ (growth) for $k < k_0$, $\gamma(k)$ has its maximum value at $k = k_0$, and $\gamma(k)$ becomes strongly negative (damping) as k becomes large.

Our numerical implementation of this CCM model employs doubly periodic boundary conditions with periodicity lengths L_x in x and L_y in y. The nonlinear

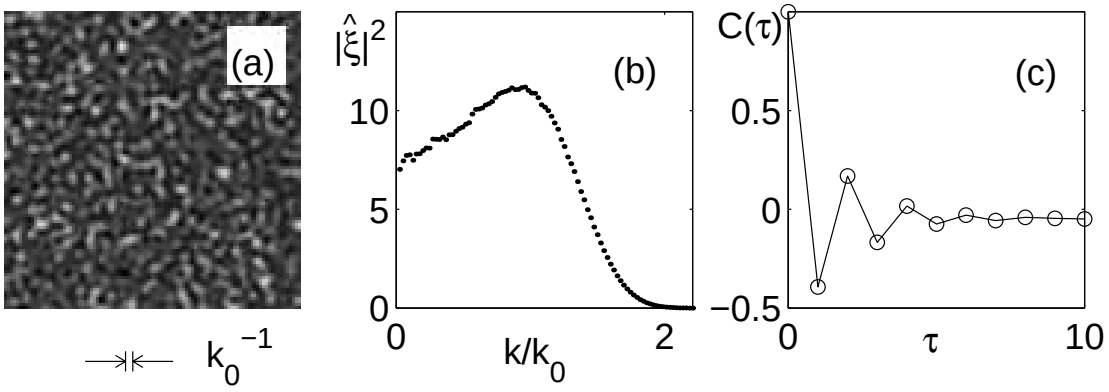

Figure 2.2: Spatiotemporal chaos of CCM model for $A = 7.0, r = 0.4$, and $w = 0.29$: (a) A snapshot of $\xi_n(\vec{x})$. Bright regions indicate large amplitude. (b) Wavenumber power spectrum, averaged over 100 frames. $\hat{\xi}(\vec{k})$ is the Fourier transformation of $\xi(\vec{x})$. (c) Time correlation function $C(\tau)$, Eq. (2.7).

map operator is applied at points on a square grid, while the spatial coupling operator (2.2) employs fast Fourier transforming from $\vec{x}$ to $\vec{k}$ and back.

That $\xi(\vec{x}) = 0$ is an attractor can be seen by introducing an initial perturbation at wavenumber $\vec{k}, \delta\xi_0 \exp(i\vec{k} \cdot \vec{x})$. Linearization of the CCM model about $\xi_0(\vec{x}) = 0$ then shows that this perturbation evolves with time to $\delta\xi_n \exp(i\vec{k} \cdot \vec{x})$, where $\delta\xi_n = \delta\xi_0[M'(0)f(k)]^n, M'(\xi) \equiv \partial M/\partial\xi$. For the parameters we choose $M'(0)f(k) < 1$ for all k (in particular $M'(0)f(k_0) < 1$). Thus the homogeneous state $\xi(\vec{x}) = 0$ is an attractor for the system. We also find that, as we had anticipated, for other initial conditions there is another attractor which is spatiotemporally chaotic.

Figure 2.2 shows the properties of the spatiotemporal chaos produced by our model. Figure 2.2(a) shows the spatial pattern $\xi_n(\vec{x})$ at a representative time. This picture applies to a time $n = 45$ evolved from an initial condition where $\xi_0(\vec{x})$ was chosen randomly with uniform distribution between $\xi_0 = 0$ and $\xi_0 = 7.5$. Visually,

we observe that the pattern appears to have a characteristic scale of the order of k_0^{-1}. This is confirmed by the wavenumber power spectrum, Fig. 2.2(b). We note that the only length scales in our model are k_0^{-1}, the system size $L \sim L_x \sim L_y$, and the grid size δ, and that, by our choice $L \gg k_0^{-1} \gg \delta$, we had sought to obtain spatiotemporal chaos with properties independent of L and δ. (In whta follows we use a definition of length such that $\delta = 1$, and we choose $k_0^{-1} = 6.3$ for all our numerics.) Figure 2.2(b), which evidences variation on the scale k_0, conforms with this expectation. Further discussion of the form observed for $|\hat{\xi}(k)|^2$ is given in the appendix. To characterize the temporal variation of the patterns, Fig. 2.2(c) shows a plot of the time correlation function $C(\tau)$ defined as

$$C(\tau) = \frac{1}{N_x N_y} \sum_{i,j}^{N_x N_y} C_{i,j}(\tau), \tag{2.6}$$

$$C_{i,j}(\tau) = \frac{< (\xi_{i,j}(t+\tau) - \bar{\xi}_{i,j})(\xi_{i,j}(t) - \bar{\xi}_{i,j}) >}{< \xi_{i,j}^2(t) - \bar{\xi}_{i,j}^2 >}, \tag{2.7}$$

where $< ... >$ means time average, $\bar{\xi} =< \xi >$, $N_{x,y} = L_{x,y}/\delta$, and (i,j) denotes the (x,y) location of a grid point. As can be seen from Fig. 2.2(c) the time correlation function decays to zero with increasing time τ (where τ is an integer), confirming that the temporal behavior is chaotic.

We have also examined other parameter values for which (2.1)-(2.5) yields spatiotemporal chaos, and we find behavior similar to that in Figs. 2.2.

2.3 Propagation of a Flat Front

The main objective of our investigation is to characterize the dynamics of the interface between a spatiotemporally chaotic state and a stable steady state. In our first set of simulations we focus on an initially flat interface, $y = y_0$ at $t = 0$.

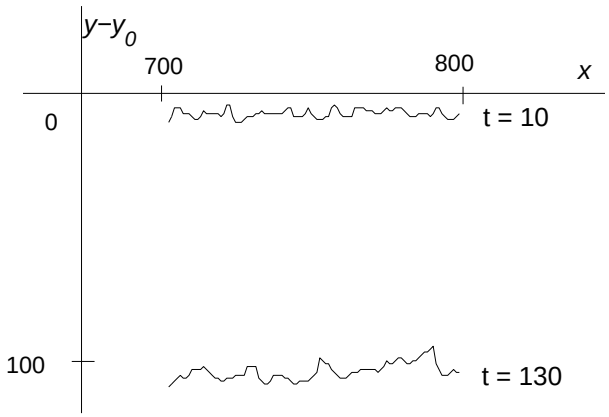

Figure 2.3: Coarsening of a flat front. $L_x = 1024$.

After we generate an initial spatiotemporally chaotic state [Fig. 2.2(a)], we create the interface by setting the amplitude ξ of all grid points with $y < y_0$ to the stable steady state value $\xi = 0$. During further iterations, the front between the chaotic and steady state moves downward, i.e., the chaotic state propagates into the stable steady state, and the front coarsens (see Fig. 2.3). In order to examine the front dynamics for long times and save computational time, we use a shifting method: On every iterate, we reset ξ to zero in the region adjacent to the bottom ($y = 0$) of the periodic box, and, when the front comes close to $y = 0$, we shift the whole system upward in the y direction. Due to the periodic boundary conditions, after this shift there will be a region below the front and above $y = 0$ that is in the spatiotemporally chaotic regime, and we then set $\xi = 0$ in this region.

After an initial transient, the scaling properties of the front are studied using the following definition of the interface width. First, we calculated the average value of ξ at fixed y, $\tilde{\xi}(y) = \int_0^{L_x} \xi(x, y)dx/L_x$. We then note that the basin boundary between the two attractors of the one dimensional map M is at the unstable fixed

point, $u = 0.4824$ (Fig. 2.1), and that the average ξ for the spatiotemporally chaotic state [Fig. 2.2(a)] is approximately four times the critical value. Thus, we define a lower boundary of the front, y_1, by $\tilde{\xi}(y_1) = u$ and an upper boundary of the front, y_2, by $\tilde{\xi}(y_2) = 3u$. The width of the front is then defined as $(y_2 - y_1)$.

Because of the inherent 'noise' generated in the spatiotemporally chaotic region, the proper quantity to study is the ensemble averaged mean of the front widths. We calculate ensembles using many different random initial conditions. Our results for the ensemble averaged width w of the front are obtained by averaging $(y_2 - y_1)$ over 10 runs for the largest system $L_x = 1024$ and over 500 runs for the smallest $L_x = 64$. The typical coarsening of the front is shown in Fig. 2.3.

One observation from our simulations is that the propagation velocity of fronts is constant, except for a few transient initial iterations. That is, the velocity does not depend on time or system size. A constant propagation front velocity is also observed in the experiments in Refs. [1] and [2]. To minimize the effect of the initial transient, we redefine time as the total increase in the area of the chaotic state.

As is typical for a front coarsening problem [4], the time and system size dependence of the mean front width w can be described by a scaling function $g(u)$,

$$w(t) = t^{\beta} g(\frac{t}{L_x^z}). \tag{2.8}$$

Here $g(u)$ is constant for $u \ll 1$ and $g(u) \approx u^{-\beta}$ for $u \gg 1$. For $t \gg L_x^z$, the width saturates at $w \sim L_x^{\alpha}$ where $\alpha = \beta z$ is the roughness exponent. Barabási and Stanley [4] have summarized the values of the scaling exponents z, α, and β that are obtained for several experimental systems as well as relevant theoretical results.

In Fig. 2.4(a), we show w versus t for different system sizes. These data show

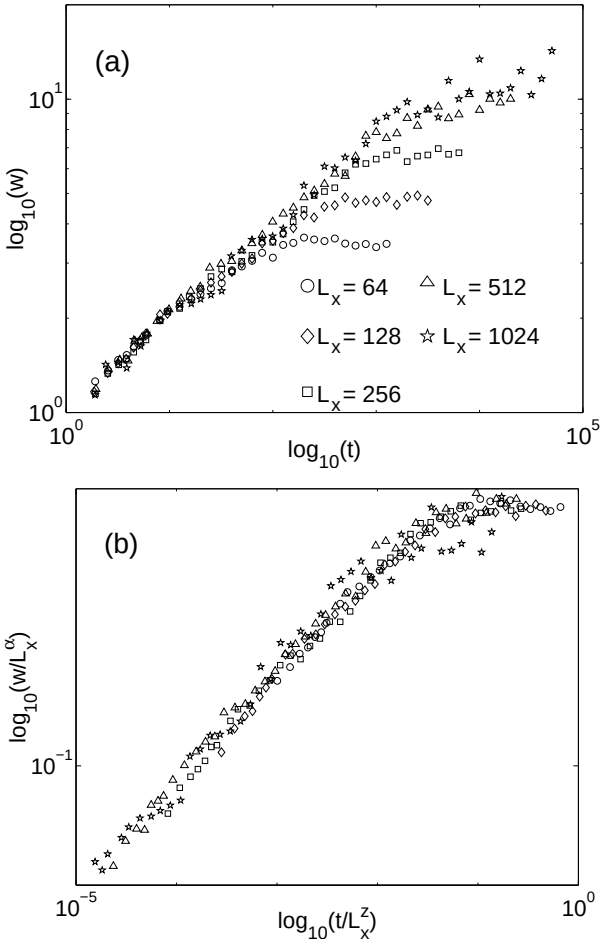

Figure 2.4: Scaling of width with the size: (a) unscaled, (b) scaled with $\alpha = 0.49, z = 1.81$ from which $\beta = \alpha/z = 0.27$. Circles ($L_x = 64$), diamonds ($L_x = 128$), squares ($L_x = 256$), triangles ($L_x = 512$), and stars ($L_x = 1024$). $L_y = 256$ for all cases.

two characteristic regimes: power law growth, followed by saturation. The growth exponent, β, is calculated by measuring the slopes of straight line fits to the data before saturation, and the roughness exponents α is calculated by comparing the saturation widths. Figure 2.4(b) shows w/L_x^{α} versus t/L_x^z, where α and z have been

adjusted to $\alpha = 0.49$ and $z = 1.81$ (corresponding to $\beta = \alpha/z = 0.27$). Consistent with Eq. (2.8), we find collapse of the data in Fig. 2.4(a) to a single scaling function. The exponent values we obtain are roughly consistent with those of both the two dimensional Eden model ($\alpha \cong 0.5, \beta \cong 0.3$) and the two dimensional Kardar-Parisi-Zhang equation ($\alpha = 1/2, \beta = 1/3$) [4, 6].

2.4 Evolution of a Non-flat Front

We now consider the evolution of a front on large length scale. Specifically, we are interested in the case where the front is initially not flat; that is, the position of the front is initially given by $y_0 = h(x_0)$. Furthermore, we assume that, as the front evolves, the scale on which the front position varies, $l \approx (h/h')$, remains large compared to the front width,

$$l \gg w. \tag{2.9}$$

To analyze this situation, we consider that a point on the front moves with a normal velocity $\vec{v}$ whose magnitude, $|\vec{v}| = v$, is constant in time. This assumption also implies that the direction of $\vec{v}$ following the trajectory of a point on the front is constant in time. This is because the slope of the front, dx/dy, following a trajectory does not change with time; i.e., it depends only on the initial location x_0 on the front and not on t. This is illustrated by the construction in Fig. 2.5(a). As shown in the figure, the trajectory line segments are straight, are all of the same length, vt, and are normal to both the initial front and to the evolved front. Considering an initial front position given by $y_0 = h(x_0)$, propagation at a velocity

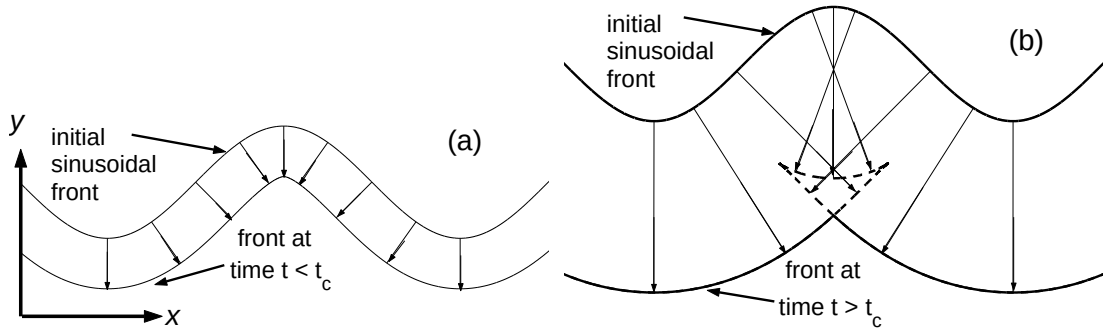

Figure 2.5: Geometrical picture of the trajectories given by Eqs. (2.10) and (2.11): (a) for $t < t_c$ and (b) for $t > t_c$.

$\vec{v}$ normal to the front then yields

$$x(t) = x_0 - (vt)h'(x_0)[1 + (h'(x_0))^2]^{-1/2}, \tag{2.10}$$

$$y(t) = h(x_0) - vt[1 + (h'(x_0))^2]^{-1/2}. \tag{2.11}$$

At any given time Eqs. (2.10) and (2.11) specify the front position parametrically with x_0 as a parameter. As an example consider the case of an initial sinusoidal undulation of the front $y_0 = h(x_0) = C\cos(kx_0)$. As the front propagates, the initial sinusoidal curve becomes distorted so that the maxima become sharp and the minima become broad. As can be seen from Fig. 2.5 (a) this arises because of the converging (diverging) of trajectories that originate near maxima (minima).

Past a critical time $t = t_c$ a cusp develops at the maxima of the evolved front [7]. The cusp formation time is determined by noting that dx/dx_0 first becomes zero at $t = t_c$. From Eq. (2.10) we obtain

$$t_c = \frac{1}{k^2 Cv}. \tag{2.12}$$

For $t > t_c$ there are pairs of values of x_0 for which the trajectories given by (2.10) and (2.11) pass through each other. For a given time t greater than t_c we refer to

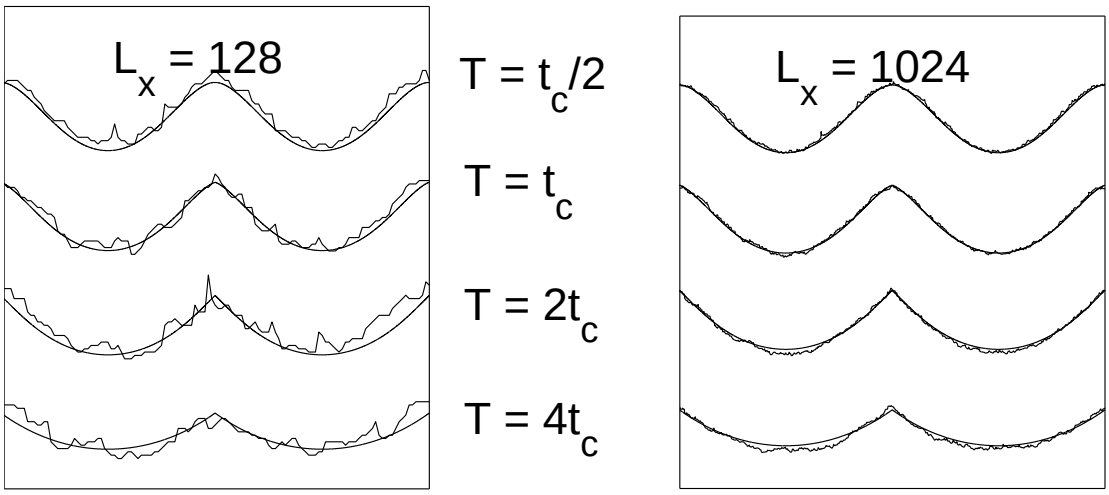

Figure 2.6: Comparison between theoretical curves and our 2D simulations for two different system sizes. The front curve from our model is defined as the smallest y value (for given x) at which $\xi = u$, where $u = 0.4824$ is the basin boundary point depicted in Fig. 2.1.

the range of x_0 for which this occurs as the unphysical range. The development of the unphysical range is illustrated in Fig. 2.5 (b) where the dashed portion of the curve shows the result of plotting (2.10) and (2.11) for the unphysical range.

Figure 2.6 shows how cusps develop in time. In Fig. 2.6 the noisy front curves are from our simulations and the smooth curves are from Eqs. (2.10) and (2.11) with x_0 restricted to the physical range. The two cases shown in Fig. 2.6 (namely, $L_x = L_y = 128$ and $L_x = L_y = 1024$) illustrate how front roughening becomes of less influence as (2.9) becomes better satisfied. For both cases in Fig. 2.6 the initial sinusoid has amplitude $kC = 1$ and wavenumber $k = 4\pi/L_x$. Thus from

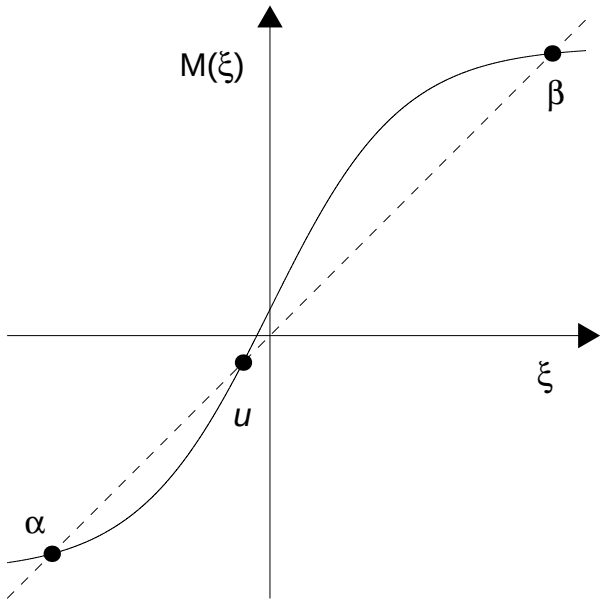

Figure 2.7: The map Eq. (2.13).

(2.12) we have $t_c \sim 1/k \sim L_x$. At times $t \sim t_c$, the roughening is a small effect if $kw(t_c)$ is small. Since $w \sim t^\beta$ (assuming $t/L_x^z \lesssim 1$), we see that $kw(t_c) \sim 1/L_x^{1-\beta}$, and roughening will be inconsequential for the large scale front evolution if L_x is sufficiently large. The good agreement of the $L_x = 1024$ numerical results from our CCM model with the theory, Eqs. (2.10) and (2.11), confirms that the front does indeed propagate at constant velocity in a direction perpendicular to the interface. In particular, for long length scales $l \gg w$ examined in Fig. 2.6 we see no evidence for curvature dependence of the front velocity.

As a comparison, we have also considered the propagation of a front between two steady homogeneous states. In particular, replacing $M(\xi)$ in Eq. 2.3 by

$$M(\xi) = 0.1 + \tanh(2\xi), \tag{2.13}$$

we see (Fig. 2.7) that there are two stable fixed points, α and β, and one unstable fixed point u. Using (2.13), (2.2) and(2.5) with a sinusoidal front with initialization

of β above the front and at α below the front, we find that the front shape evolves smoothly (with no roughening) according to Eqs. (2.10) and (2.11). Thus the cases of a chaotic invading region and a nonchaotic invading region become similar for large L_x (e.g., $L_x \gg w \gg 1/k_0$).

2.5 Summary

We have introduced a continuum coupled map model for the study of the dynamics of a front separating a region of spatiotemporal chaos from a stable steady region. This model is applicable to periodically forced systems. We find that the front roughens and that this coarsening obeys a scaling hypothesis, Eq. (2.8). We also investigate the large length scale evolution of a nonplanar front. We find that this evolution is consistent with the hypothesis that, on large scale, the front velocity is constant and normal to the front. This hypothesis and our numerical simulations indicate the formation of cusp structures in the front.

Appendix

We now comment on the specific form that we have found for $|\hat{\xi}|^2$ (Fig. 2.2(b)). In this connection we note that in the limit of a wildly varying map $M(\xi)$ with Lyapunov exponent approaching infinity $\xi'_n(\vec{x})$ will be wildly varying in space. This is because small variation of $\xi_n(\vec{x})$ with $\vec{x}$ are greatly amplified when M is applied. Thus, in this limit, the spatial correlation function for $\xi'_n(\vec{x})$ will be a delta function, and $|\hat{\xi'}_n(k)|^2 =< (\xi'_n(\vec{x}))^2 >$ independent of $\vec{k}$. Thus from (2.2)

$$|\hat{\xi}(k)|^2 =< (\xi'_n(\vec{x}))^2 > f^2(k), \qquad (A.1)$$

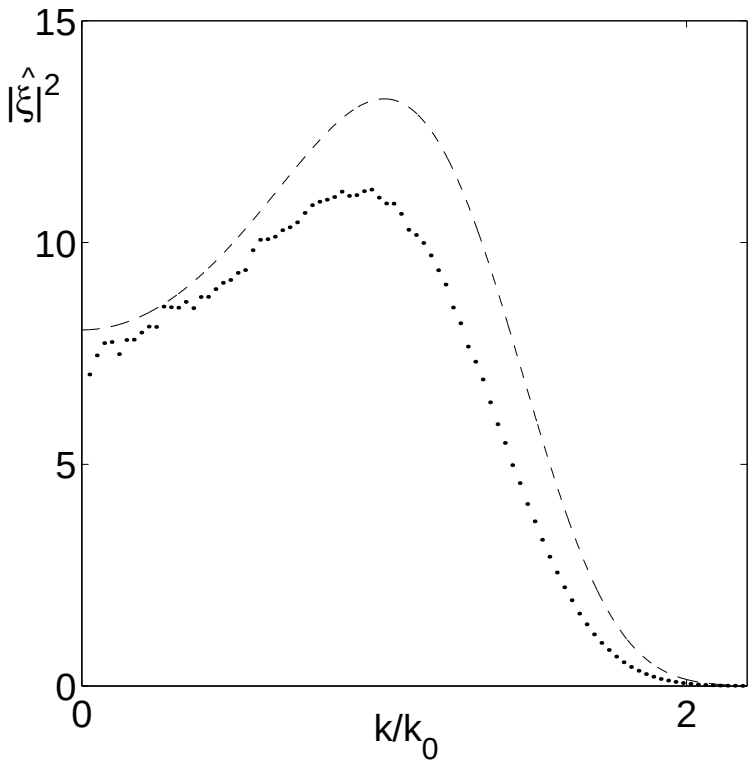

Figure 2.8: $|\hat{\xi}|^2$ versus k compared with Eq. (A.1).

which is plotted in Fig. 2.8 as the dashed line along with the data from Fig. 2.2(b). It is seen that Eq. (A.1) provides a crude indication of the general form of $|\hat{\xi}(k)|^2$.

Chapter 3

Rare Intense Events

3.1 Preview

Many spatiotemporal dynamical systems show rare intense events. One example is that of large height rogue ocean waves [8]. Another example occurs in recent experiments on parametrically forced surface waves on water in which high spikes (bursts) on the free surface form intermittently in space and time [9]. Other diverse physical examples also exist (*e.g.*, tornados, large earthquakes, etc.). The characteristic feature of rare intense events is an enhanced tail in the event size probability distribution function. Here, by enhanced we mean that the event size probability distribution function approaches zero with increasing event size much more slowly than is the case for a Gaussian distribution. Thus these events, although rare, can be much more common than an expectation based on Gaussian statistics would indicate. The central limit theorem implies Gaussian behavior for a quantity that results from the linear superposition of many random independent contributions. Non-Gaussian tail behavior can result from strong nonlinearity of the events, and enhancement of the event size tail might be expected if large amplitudes are nonlinearly self-reinforcing. Such nonlinear self-reinforcements is present

in the nonlinear Schrödinger (NLS) equation. In particular, the two dimensional NLS equation,

$$\frac{\partial A}{\partial t} = -i\alpha|A|^2 A - i\beta \bigtriangledown^2 A. \tag{3.1}$$

exhibits "collapse" when the coefficients α and β have the same sign [10]. In a collapsing NLS solution the complex field approaches infinity at some point in space, and this singularity occurs at finite time. The NLS is conservative in that it can be derived from a Hamiltonian, $\partial A/\partial t = -i\delta H/\delta A^*$, where $H[A, A^*] = \frac{1}{2}\int[\alpha|A|^4 + \beta|\bigtriangledown A|^2]d\mathbf{x}$. In the case of nonconservative dynamics, inclusion of lowest order dissipation and instability terms leads to the complex Ginzburg-Landau (CGL) equation [11]. The CGL equation has been studied as a model for such diverse situation as chemical reaction [12], Poiseuille flow [13], Rayleigh-Bénard convection [14], and Taylor-Couette flow [15]. In the limit of zero dissipation/instability the CGL equation approaches the NLS equation. For small nonzero dissipation/instability, the CGL equation displays a solution similar to the NLS collapse solution, but with a large finite (rather than infinite) amplitude at the collapse time [10]. Furthermore, over a sufficiently large spatial domain, these events occur intermittently in space and time. Thus, in this parameter regime, the CGL equation may be considered as a model for the occurrence of rare intense events.

In this chapter we study the statistics and characteristics of rare intense events in a two-dimensional CGL-based model. The probability distribution function (PDF) of the amplitude of the solutions is observed to be non-Gaussian in our numerical experiments. This non-Gaussian PDF is explained by the nonlinear characteristics of individual bursts combined with the statistics of bursts. The

model equation we investigate is

$$\begin{aligned} \frac{\partial A}{\partial t} &= \pm A - (1+i\alpha)|A|^2 A + (1-i\beta) \bigtriangledown^2 A \\ &\quad +(\delta_r + i\delta_i)A^*, \end{aligned} \tag{3.2}$$

where $(\delta_r + i\delta_i)A^*$ is a parametric forcing term [16]. We will consider two cases: one without parametric forcing ($\delta_r = \delta_i = 0$) in which case the plus sign is chosen in front of the first term on the right-hand side of (3.2) (Eq. (3.2) is then the usual CGL equation), and one with parametric forcing, in which case the minus sign is chosen. As previously discussed, we choose our parameters so that our model, Eq. (3.2), is formally close to the NLS equation (3.1). That is, we take $\alpha, \beta \gg 1, \delta_r, \delta_i$, and for our numerical solutions we will restrict attention to the case $\alpha = \beta$. Note that the coefficient ± 1 for the first term, as well as the ones in $(1+i\alpha)$ and $(1+i\beta)$ represent no loss of generality, since these can be obtained by suitable scaling of the time (t), the dependent variable (A), and the spatial variable ($\mathbf{x}$). In Section 3.2, we discuss the amplitude statistics of our two-dimensional CGL models with and without the parametric forcing term. We find that the PDFs are approximately described by a stretched exponential distribution, $P(|A|) \approx \exp(-|A|^\eta)$, where η is less than 1. In Section 3.3, we investigate the characteristics of individual bursts. We compare our numerical CGL results with known collapse solutions of the NLS equation. The maximum amplitude obtained by many bursts (or the "event size" statistics) is discussed in Section 3.4. Section 3.5 presents further discussion and conclusions.

Our results lead us to the following picture for the occurrence of rare intense events in our system. Linear instability and nonlinear wave saturation lead to an incoherent background of small amplitude waves. This background is responsible for the observed *small* $|A|$ Gaussian behavior of our probability distribution

functions. When, by chance, the weakly interacting waves locally superpose to create conditions enabling nonlinear, coherent self-reinforce, a localized, collapse-like event is initiated. Collapse takes over, promoting large, rapid growth and spiking of A. This is followed by a burn-out phase in which the energy in rapidly dissipated due to the generation of small scale structure by the spike. We believe that elements of the above general picture may be relevant to a variety of physical situations where rare intense events occur (*e.g.*, the parametrically driven water wave experiments in Ref. [9]).

3.2 Amplitude Statistics

3.2.1 2D model without a parametric force ($\delta_r = \delta_i = 0$)

We first consider Eq.(3.2) with $\delta_r = \delta_i = 0$ and with the plus sign in the first term on the right hand side of the equation. Figure 3.1(a) shows a representation of $|A(\mathbf{x}, t)|$ [from numerical solution of Eq. (3.2)] at a fixed instant t, where large values are indicated by darker grey shades. As a function of time, the localized dark shades occur in an seemingly random manner, become darker (*i.e.,* increase their amplitude) and then go away (become light). Furthermore, the maximum amplitudes also display apparent randomness. [see Fig. 3.1(b)]. As shown in the next section (Sec. 3.3), although the occurrence of these intense events is apparently erratic in time and space, individually these events are highly coherent. In this section, we will study the statistical properties of $A(\mathbf{x}, t)$.

Our numerical solutions of (3.2) employ periodic boundary conditions on a 256×256 grid. We choose the parameters, α and β, large enough ($\alpha = \beta = 30$) so that the solutions of our model are close to solutions of the NLS equation.

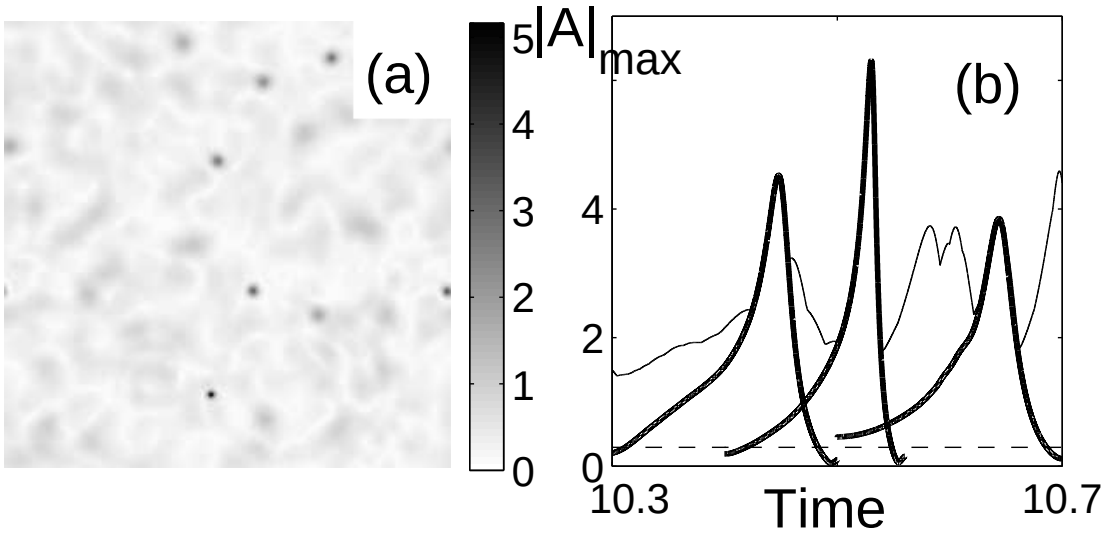

Figure 3.1: Solutions of the CGL model. (a) Snapshot of the amplitude $|A|$ for $L = 20\pi$, $\alpha = \beta = 30$, $\Delta t = 10^{-5}, \delta_r = \delta_i = 0$ and a 256×256 grid. (b) Amplitude profile versus time. Solid line indicates $|A|_{max}$ of the whole system, while thick solid lines indicate maximum amplitude of the localized events("bursts"). The dashed line indicates the average amplitude of $|A|$ over the whole system $|A|_{avg} \sim 0.3$.

We choose the time step small enough to satisfy the condition for unconditional stability of our second-order accurate time integration($\Delta t = 10^{-5}$). We use random initial condition (at $t = 0$, we generate random values for amplitudes and phases at each grid point). Localized structures, "bursts", develop very rapidly and occur throughout the spatial domain. The typical life time of a burst (δt) is approximately 0.2 time units. The maximum amplitudes of bursts are different for different burst events.

Imagining that we choose a space-time point $(\mathbf{x}, t)$ at random, we now consider the probability distribution functions for $|A|$ (the magnitude of A), $A_r = Re[A]$ (the real part of A), and $A_i = Im[A]$ (the imaginary part of A). We denote these

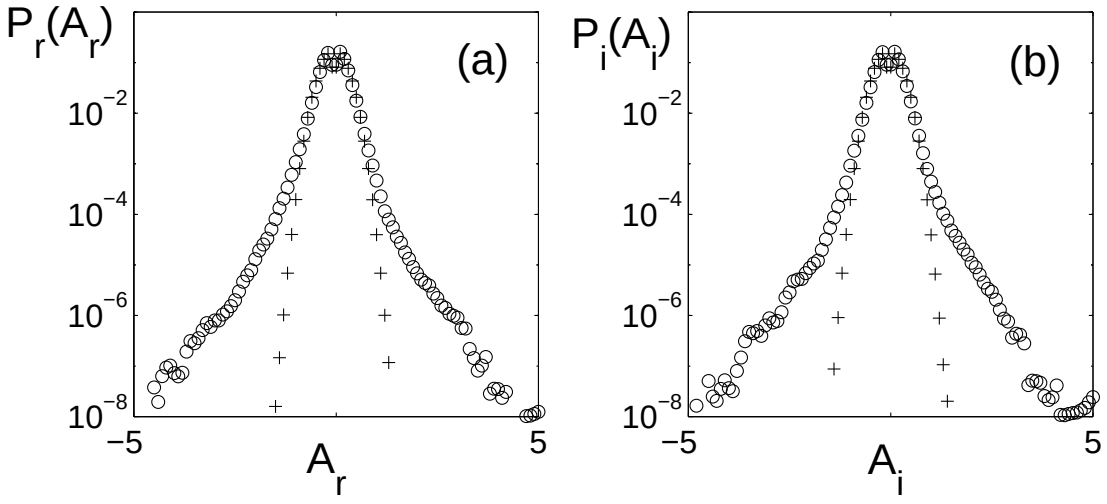

Figure 3.2: Probability distribution functions obtained from numerical solution of Eq.(3.2) using the same parameters as in Fig. 3.1. The circles are data for P_r and P_i, while the pluses are the probability distributions P_r' and P_i' obtained from the phase randomized amplitude.

distribution functions $P(|A|), P_r(A_r), P_i(A_i)$, and we compute them via histogram approximations using the values of $|A|, A_r$, and A_i from each of the 256×256 grid points at many time frames [17]. We find that these distributions are independent of the periodicity length L used in the computation as long as it is sufficiently large compared to the spatial size of a burst, but is not so large that spatial resolution on our 256×256 grid becomes problematic. In our computations of P, P_r and P_i, we choose $L = 20\pi$.

Figures 3.2 show the numerically computed probability distributions $P_r(A_r)$ [Fig. 3.2(a)] and $P_i(A_i)$ [Fig. 3.2(b)] plotted as open circles. Since Eq. (3.2) with $\delta_r = \delta_i = 0$ is invariant to the transformation $A \rightarrow A\exp(i\phi)$ (where ϕ is an arbitrary constant), we expect the distribution P_r and P_i to be the same to within

the statistical accuracy of their determinations. This is born out by Figs. 3.2. In order to highlight the essential role that nonlinearity plays in determining these distribution functions, we have also computed them after randomizing the phases of each Fourier component. That is, representing $A(\mathbf{x}, t)$ as

$$A(\mathbf{x}, t) = \sum_{\mathbf{k}} a_{\mathbf{k}}(t) \exp(i\mathbf{k} \cdot \mathbf{r}), \tag{3.3}$$

where $\mathbf{k} = (2m\pi/L, 2n\pi/L)$, we form a new amplitude, $A'(\mathbf{x}, t)$ as

$$A'(\mathbf{x}, t) = \sum_{\mathbf{k}} a_{\mathbf{k}}(t) \exp(i\mathbf{k} \cdot \mathbf{r} + i\theta_{\mathbf{k}}), \tag{3.4}$$

where for each $\mathbf{k}$, the angle $\theta_{\mathbf{k}}$ is chosen randomly with uniform probability density in $[0, 2\pi]$. The probability distribution functions for the real and imaginary parts of the randomized amplitudes A' are shown as pluses in Figs. 3.2. Note that by construction, A and A' have identical wavenumber power spectra. Due to the random phases, A' at any given point $\mathbf{x}$ can be viewed as a sum of many independent random numbers (the Fourier components). Hence the P_r and P_i distributions are expected to be Gaussian, $\log P_{r,i} \sim [(const.) - (const.)A_{r,i}^2]$. This is confirmed by the semi-log plots of Figs. 2, where the data plotted as pluses can be well-fit by parabolae.

The above comparisons with the phase randomized variable A' are motivated by imagining the hypothetical situation where the amplitude is formed by the superposition of many noninteracting linear plane waves. In that case we would have an amplitude field of form

$$\sum_{\mathbf{k}} b_{\mathbf{k}}(t) \exp(i\mathbf{k} \cdot \mathbf{r} + i\omega_{\mathbf{k}} t). \tag{3.5}$$

Because $\omega_{\mathbf{k}}$ is different for different $\mathbf{k}$, the phases become uncorrelated for sufficiently large time t.

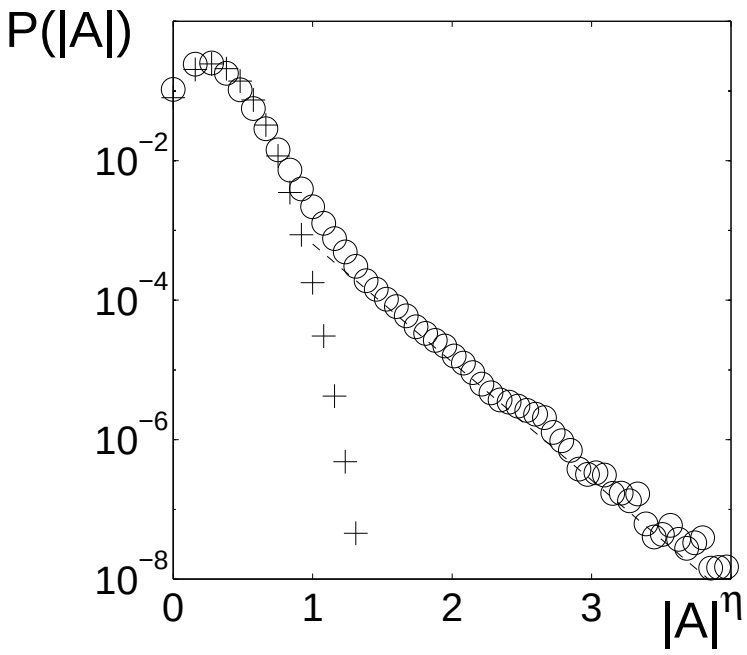

Figure 3.3: Probability distribution functions before randomizing the phases of the solutions (o) and after randomizing the phases (+). Note the horizontal axis is $|A|^\eta$, where the exponent $\eta = 0.8$ is chosen to yield approximately linear dependence of $\log[P(|A|)]$ on $|A|^\eta$ for large values of $|A|$.

Comparing the data from A and A' in Figs. 3.2, for small values of A_r and A_i, the PDFs are nearly Gaussian. This can be attributed to near linear behavior of small amplitude waves. On the other hand, for the tails of the distributions, we note substantial enhancement relative to the Gaussian distributions. These must be due to coherent phase correlations resulting from nonlinear interaction of different wavenumber components of A. Such phase coherence is implied by the observed coherent localized burst structures.

Figure 3.3 shows the numerically obtained distribution $P(|A|)$ plotted as circles and the probability distribution for the phase randomized amplitude $|A'|$ plotted

as pluses. Again, the enhancement of the large amplitude tail is evident. Note that the vertical axis in Fig. 3.3 is logarithmic, while the horizontal axis is $|A|^{\eta}$. Here we choose the power $\eta = 0.8$ so that the large $|A|$ data in this plot are most nearly fit by a straight line. That is, we attempt to fit $P(|A|)$ using a stretched exponential. The slope of the dashed straight line in the figure is chosen to match the large $|A|$ data. Thus, over the range of $|A|$ accessible to over numerical experiment, we find that the enhanced large $|A|$ tail probability density is roughly fit by a stretched exponential,

$$P(|A|) \sim \exp(-\zeta |A|^{0.8}). \tag{3.6}$$

3.2.2 2D model with parametric forcing ($\delta_r, \delta_i \neq 0$)

We now report similar results for the case of parametric forcing, Eq. (3.2) with $\delta_r, \delta_i \neq 0$ and the minus sign chosen in the first term on the right side of (3.2). In this case, instability of small amplitude waves is caused by the parametric forcing (nonzero $\delta_{r,i}$) and the $-A$ term represents a linear wavenumber independent damping. This model for parametric forcing was introduced [18] and has been used to model various situations. One such situation is that of periodically forced chemical reactions [19]. Our motivation for considering this model is the Faraday experiments on strong parametric forcing of surface water waves in Ref. [9]. In that work intermittent formation of large localized surface perturbations results in splash and droplet formation.

Parameters for our numerical simulations are the same as in Sec. 3.2.1 except that now $\delta_r = \delta_i = 5$. Again coherent localized structures, "bursts", develop rapidly and occur intermittently throughout the spatial domain, Fig. 3.4(a). As in Sec. 3.2.1, the typical life time of a burst is less than 0.2 time units, and the

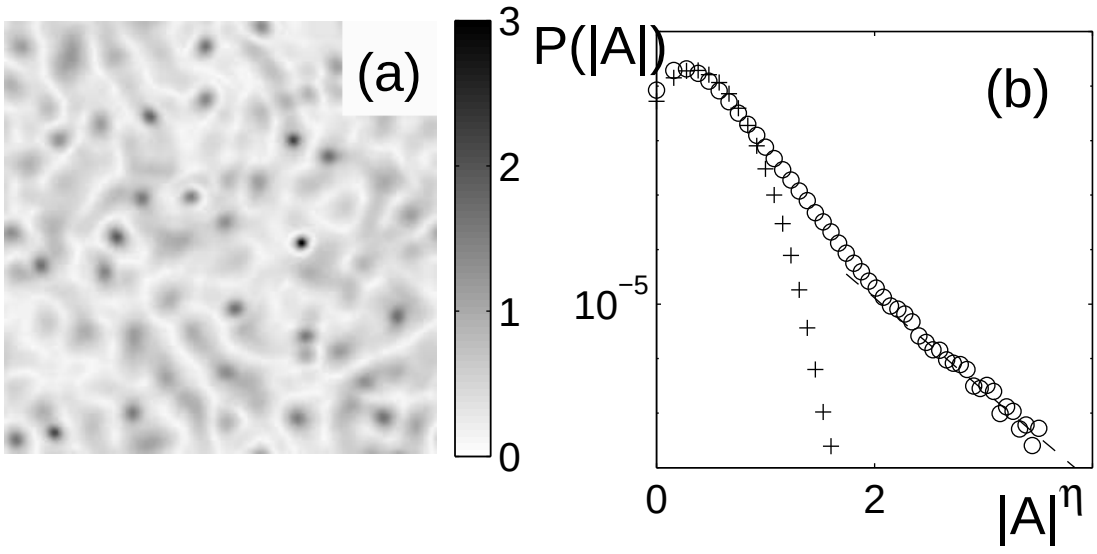

Figure 3.4: Solutions of the model with parametric forcing. (a) snapshot of $|A|$. Dark regions have high amplitudes. (b) $P(|A|)$ versus $|A|^{\eta}$, where $\eta = 0.8$. (See captions in Fig. 3.3.)

maximum amplitudes of bursts are different for different bursts.

The PDF, $P(|A|)$ again shows a stretched exponential tail with exponent $\eta = 0.8$, Fig. 3.4(b). The circles in Figs. 3.5 show the PDFs of the real and imaginary parts of A, while the pluses are data for the PDFs after randomizing the phase. The shape of the PDFs around the central part are nearly Gaussian. In contrast, at large amplitude the PDFs are significantly non-Gaussian. A major difference with the case $\delta_r = \delta_i = 0$ is that, with parametric forcing, the model is not invariant to $A \to Ae^{i\phi}$, and thus P_r and P_i may be expected to evidence differences not present for $\delta_r = \delta_i = 0$. This is seen to be the case in Figs. 3.5.

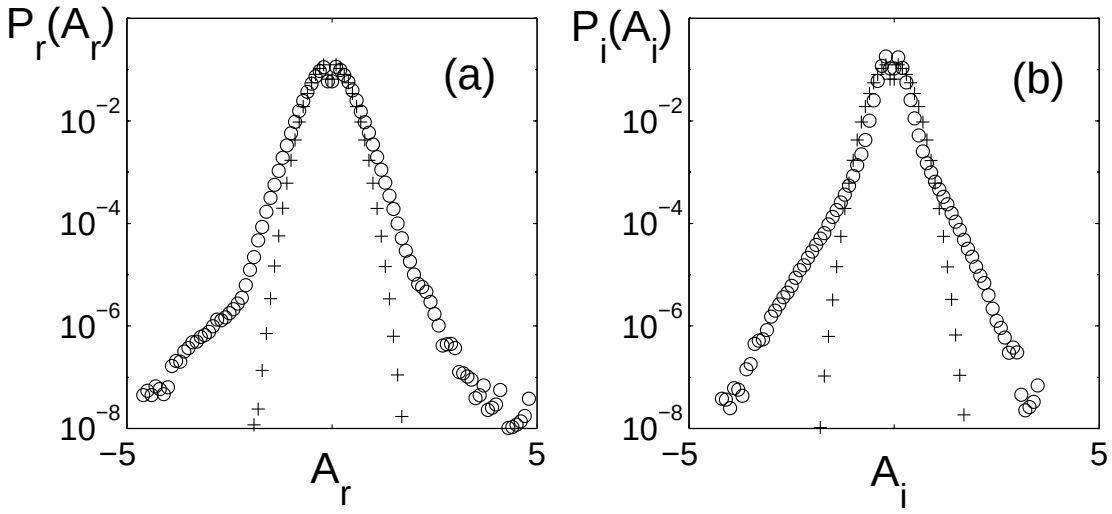

Figure 3.5: $P_r(A_r)$ and $P_i(A_i)$ with parametric forcing. The numerical parameters are the same as those for Fig. 3.4. The circles are PDFs for A_r and A_i before randomizing the phases of the solutions, while pluses are PDFs after randomizing the phases.

3.3 Characteristics of Individual Burst Events

Solutions of the CGL equation with large α and β may be expected to have features in common with solutions of the NLS equation. It is known that the NLS equation yields localized events which develop finite time singularities where the amplitude becomes infinite [11]. While it is difficult to understand the dynamics of the solutions of CGL equation from direct rigorous analysis, the solutions of the NLS equation are relatively well understood. Thus, we analyze the dynamics of individual CGL bursts guided by the known localized self-similar collapsing solution of the NLS equation.

The NLS equation has a special solution [20] of the form

$$A = e^{i\theta t} R(r), \qquad r = \sqrt{x^2 + y^2}, \tag{3.7}$$

where the radial function $R(r)$ satisfies

$$\left(\frac{\partial^2}{\partial r^2} + \frac{1}{r}\frac{\partial}{\partial r}\right) R - \xi R + R^3 = 0, \tag{3.8}$$
$$\left|\frac{\partial R}{\partial r}\right|_{r=0} = 0, \quad R(\infty) = 0,$$

where $\alpha = \beta$, $\xi = \theta/\beta$. Since (3.1) is invariant under the scaling transformation [21],

$$A(\mathbf{x}, t) \longrightarrow L(t)^{-1} A(\kappa, \tau) \mathrm{e}^{iL\dot{L}|\kappa|^2/4}, \tag{3.9}$$

where $L(t)$ tends to zero as $t^* \longrightarrow t$, $t < t^*$ and

$$\kappa = \frac{\mathbf{x}}{L(t)}, \qquad \tau = \int_0^t \frac{1}{L^2(s)} ds, \tag{3.10}$$

a family of collapsing solutions of the NLS is given by the rescaled solution of Eq. (3.8).

With these considerations, we test the expected approximate self-similarity of individual bursts observed in our numerical solutions of Eq. (3.2). We consider three typical bursts that occur at different times and spatial positions. In particular, we choose these three as the three dark regions in Fig. 3.1(a) whose spatial maxima have the time dependences shown as thick solid lines in Fig. 3.1(b).

In Fig. 3.6(a) we plot the x-dependence of $|A|$ at constant y for each of these bursts at the time that they reach their maximum amplitude (the positions in x of the maxima have been shifted to $x = 0$ and the constant y value for each is at the location of $|A|_{max}$). Note that, when they reach their maxima, the three bursts have different amplitudes and width. We rescale the amplitude and spatial

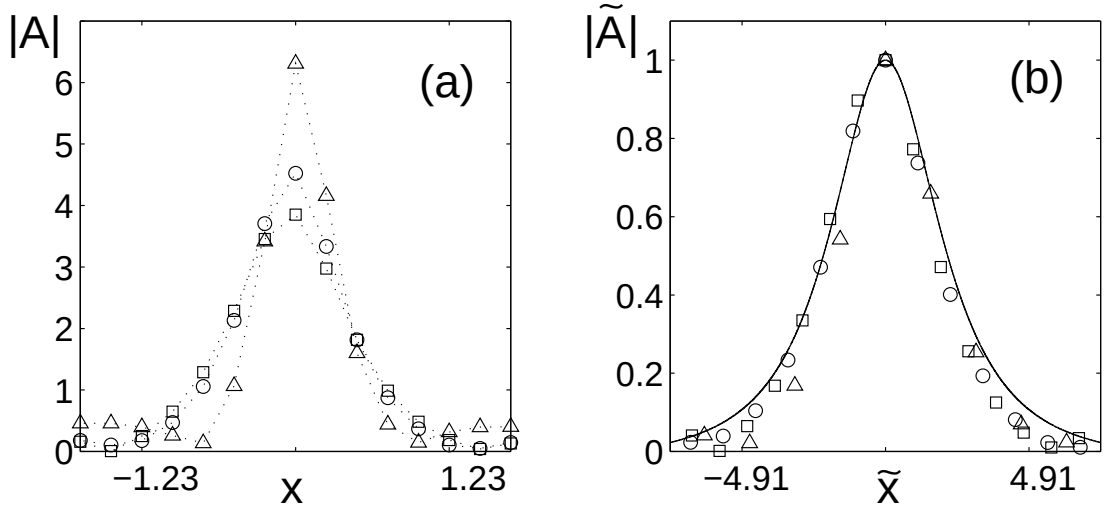

Figure 3.6: Self-similar bursts. (a) Enlarged plots of a burst at $t_1(\bigcirc) = 10.448$, at grid point $(x, y) = (15.2, 22.1)$, and $t_2(\triangle) = 10.530$, at grid point $(51.1, 25.5)$, and $t_3(\square) = 10.644$ at grid point $(57.4, 38.8)$. (b) Scaled profiles, where $|\tilde{A}| = |A|/L$, $\tilde{x} = x/L$, and $L = |A|_{max}$ at t_1, t_2, and t_3. The solid line represents the radial solution of Eq. (3.8).

coordinate as suggested by (3.9) and (3.10), $|\tilde{A}| = |A|/L$ and $\tilde{x} = x/L$, and we take $L = |A|_{max}$ (which normalizes $|\tilde{A}|_{max}$ to one). The resulting data are plotted in Fig. 3.6(b) along with the solution of Eq. (3.8). [We again rescale $R(r)$ using (3.9) and (3.10), and we note that, after this rescaling, the result is independent of the value of $\xi = 0.1$ in Eq. (3.8).] The three burst profiles show evidence of collapsing onto the theoretical radial solution.

Now, we consider the time dependence of a single burst. We select the burst at the grid point $(x, y) = (51.1, 25.5)$ (see caption to Fig. 3.6) and investigate the evolution of its shape and height. We display profiles of the burst at 5 different times in Fig. 3.7(a). Rescaling each profile using Eq. (3.9) and Eq. (3.10), and

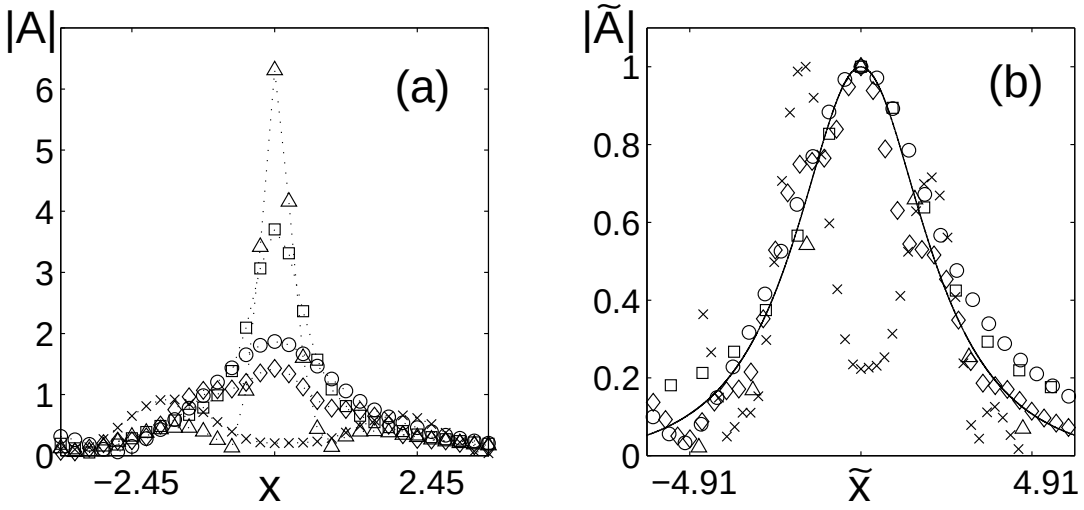

Figure 3.7: Self-similarity of single burst. (a) Enlarged plots of a burst at $t_1(\bigcirc) = 10.50$, $t_2(\square) = 10.52$, $t_3(\triangle) = 10.53$, $t_4(\diamond) = 10.54$, and $t_5(\times) = 10.55$. (b) Scaled profiles, where $|\tilde{A}| = |A|/L$, $\tilde{x} = x/L$, and $L = |A(r)|_{max}$ at t_1, t_2, t_3, and t_4. The solid line represents the solution of Eq. (3.8).

defining L in the same way as before, the four profiles at the first four times approximately collapse onto the radial solution of (3.8) as shown in Fig. 3.7(b). When the burst reaches its maximum amplitude, the amplitude at some distance away from the center becomes zero (see the amplitude profile at $t = t_3$). After that, the center decays very rapidly (see the amplitude profile at $t = t_5$). (Note that in this section and the next section, we present numerical results for (3.2) with $\delta_r = \delta_i = 0$. However, we have also verified that the CGL model with parametric forcing also has similar self similarity properties.)

3.4 Statistics of Bursts

The self similar properties of bursts implies that the solutions of the CGL model consist of self-similar bursts of various maximum heights. Thus, we expect that the enhanced tail (the deviation from the Gaussian distribution) of the amplitude probability distribution $P(|A|)$ can be understood by the statistics of bursts. In particular, we consider $g(h)$, the frequency of bursts which have maximum height h, and a distribution $P_j(|A|)$ defined for an individual burst (burst j), as follows.

We define the time interval for each burst as the time between when its peak value exceeds $2|A|_{avg}$ and when its peak value drops below $2|A|_{avg}$ [typically the time duration of a burst is less than 0.2, see Fig. 3.1(b)]. Here $|A|_{avg}$ is the space average of $|A|$ over the entire spatial grid of the simulation at each time t [$|A|_{avg}$ is approximately constant at about 0.3 over all time steps in the simulation, see the dashed line in Fig. 3.1(b)]. Consistent with the observation that a typical burst has radial symmetry, we define the domain of the burst to be a circular region of radius r_{eff} centered at the burst maximum, where r_{eff} is the maximum radius of a circle such that the average of $|A|$ over the perimeter of the circle is greater than $2|A|_{avg}$ (typically, $1.23 \leq r_{eff} \leq 4.91$). In Fig. 3.8(a) we show the distribution $P_j(|A|)$ for the three bursts in Fig. 3.1(b) (thick solid lines). The first burst ($j = 1$) has $h = 4.52$ and is plotted as the open circles in Fig. 3.8(a); the second burst ($j = 2$) has $h = 6.31$ and is plotted as the open triangles; and the third burst ($j = 3$) has $h = 3.85$ and is plotted as the open squares. These distributions are obtained from histograms of the values of $|A|$ at grid points in the domains and time steps in the duration of each of these bursts. We obtain $g(h)$ by counting the number of bursts which have maximum heights between h and $h + \Delta h$, where $\Delta h = 0.1$ [see Fig. 3.8(b)]. (In Fig. 3.8(a) $P_j(|A|)$ is not plotted for $|A| < 2|A|_{avg}$,

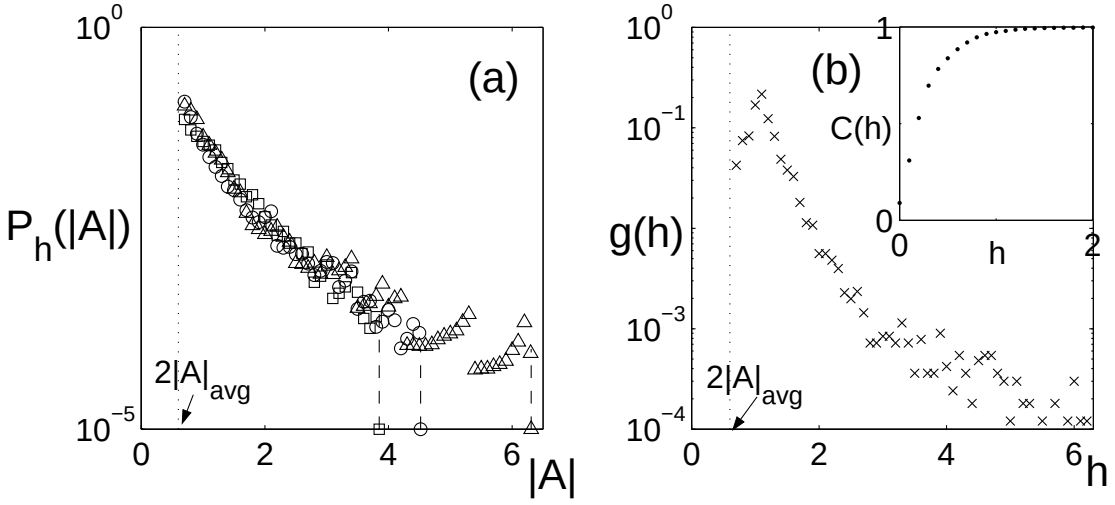

Figure 3.8: Statistics of localized events("bursts"). (a) $P_{h_j}(|A|)$ at three different times: $t_1(\bigcirc) = 10.448$ and $h = 4.52$, $t_2(\triangle) = 89.0$ and $h = 6.31$, and $t_3(\square) = 94.0$ and $h = 3.85$. (b) The frequency of bursts which have maximum height h, $g(h)$. The inset indicates $C(h)$ versus h defined in Eq. (3.13).

since, by our procedure this range lacks meaning, and since we are interested in the behavior at large values of $|A|$.) We note that the $P_j(|A|)$ in Fig. 3.8 all approximately coincide for $|A| < h$. Thus the only characteristic of the bursts on which $P_j(|A|)$ depends is the maximum burst amplitude h at which $P_j(|A|)$ goes to zero. To incorporate this fact, we replace $P_j(|A|)$ by the notation $P_h(|A|)$.

The above suggests that $P(|A|)$ can be obtained from the following approximation [22]

$$P(|A|) \sim \int_0^\infty g(h) P_h(|A|) dh, \tag{3.11}$$

where $P_h(|A|)$ is a probability distribution of a single burst whose temporal maximum amplitude is h. Since $P_h(|A|)$ vanishes for $|A| > h$ and because the $P_h(|A|)$

approximately coincide for $|A| < h$ [see Fig. 3.8(a)], we approximate $P_h(|A|)$ as

$$P_h(|A|) \sim C^{-1}(h)\theta(h-|A|)P_*(|A|), \tag{3.12}$$

$$C(h) = \int_0^h P_*(|A|)d|A|, \tag{3.13}$$

where $C(h)$ is a normalization factor [$C(h) \sim 1$, when $h > 1$; see the inset on Fig. 3.8(b)], $\theta(h-|A|)$ is a step function, and P_* is the distribution that we numerically compute at the largest value of h that we considered ($h_{max} = 6.31$). Using (3.11) and (3.13), we can further approximate $P(|A|)$ as

$$\begin{aligned} P(|A|) &\sim \int_0^\infty C^{-1}(h)\theta(h-|A|)g(h)P_*(|A|)dh \\ &\sim P_*(|A|)\int_{|A|}^\infty C^{-1}(h)g(h)dh. \end{aligned} \tag{3.14}$$

(The integral in (3.14) is the cumulative frequency of bursts which have maximum height greater than $|A|$.)

Figures 3.8 show the numerically obtained $g(h)$ and $P_*(|A|)$. Inserting $P_*(|A|)$ into Eq.(3.13) and Eq.(3.14), we obtain the prediction for $P(|A|)$ plotted as pluses in Fig. 3.9 for $|A| > 2|A|_{avg}$. This appears to agree well with the $P(|A|)$ obtained from our numerical solutions of (3.2) (open circles). (Note that we shift the predicted $P(|A|)$ (pluses) to the $P(|A|)$ (open circles) obtained from (3.2) after removing data points for $|A| < 2|A|_{avg}$.)

3.5 Summary

We find that the large A behavior of the PDF obtained from our CGL solutions is approximately described by a stretched exponential form, $P(|A|) \approx e^{-|A|^\eta}$, where $\eta < 1$. In addition, for small A, $P_r(A_r)$ and $P_i(A_i)$ are approximately Gaussian, as is the case for a random linear superposition of waves. We also observe the

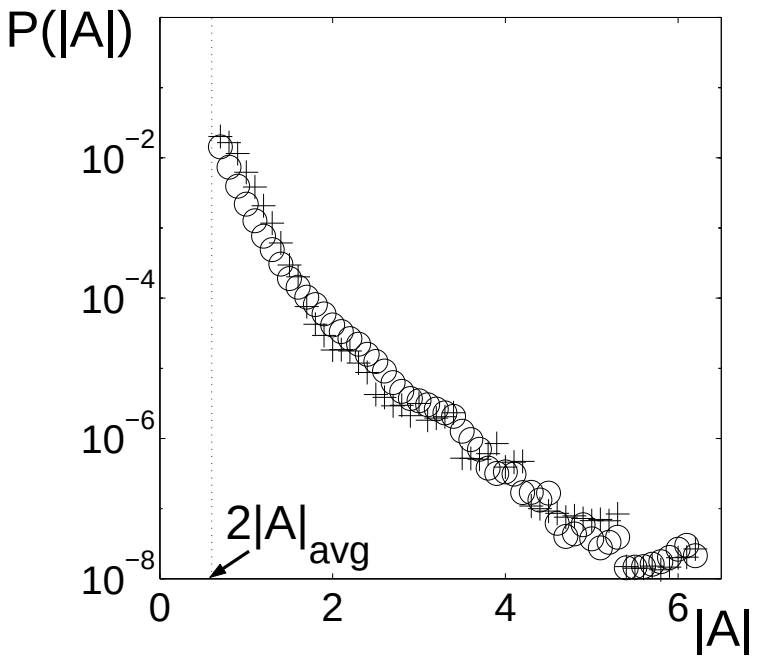

Figure 3.9: $P(|A|)$ versus $|A|$. Circles represent $P(|A|)$ obtained directly from our numerical solutions of (3.2), while pluses represent $P(|A|)$ obtained using $P_*(|A|)$ and $g(h)$ from Fig. 3.8, and Eqs. (3.11)-(3.14).

self similar properties of individual bursts, which allow us to consider the large amplitude behavior of our CGL solutions as composites of coherent self similar bursts. Based on this we explain the observed non-Gaussian $P(|A|)$ using the nonlinear characteristics of individual bursts $P_h(|A|)$ combined with the statistics of burst occurrences $g(h)$.

These results lead us to conjecture the following picture of rare intense events in our model. Linear instability leads to a background of relatively low amplitude waves that are weakly interacting and result in a random-like, incoherent background and low $|A|$ Gaussian behavior of $P_r(A_r)$ and $P_i(A_i)$. When, by chance, this incoherent behavior results in local conditions conducive to burst formation,

nonlinear, coherent, self-reinforcing collapse takes over and promotes a large growth and spiking of A. We believe that this general mechanism may be operative in a variety of physical situations in which rare intense events occur (*e.g.*, the water wave experiments of Ref. [9]).

Chapter 4

Growing Networks

4.1 Preview

It is known that many evolving network systems, including the world wide web, as well as social, biological, and communication systems, show power law distributions. In particular, the number of nodes with k links is often observed to be $n_k \sim k^{-\nu}$, where ν typically varies from 2.0 to 3.1 [23]. The mechanism for power-law network scaling was addressed in a seminal paper by Barabási and Albert (BA) who proposed [24] a simple growing network model in which the probability of a new node forming a link with an old node (the "attachment probability") is proportional to the number of links of the old node. This model yields a power law distribution of links with exponent $\nu = 3$. Many other works have been done extending this the model. For example Krapivsky and Redner [25] provide a comprehensive description for a model with more general dependence of the attachment probability on the number k of old node links. For attachment probability proportional to $A_k = ak + b$ they found that, depending on b/a, the exponent ν can vary from 2 to ∞. Furthermore, for $A_k \sim k^\alpha$, when $\alpha < 1$, n_k decays faster than a power law, while when $\alpha > 1$, there emerges a single node which connects to

nearly all other nodes. Other modifications of the model are the introduction of aging of nodes [26], initial attractiveness of nodes [27], the addition or re-wiring of links [28], the assignment of weights to links [29], etc.

We have attempted to construct more general growing network models featuring two effects which have not been considered previously: (i) multiple species of nodes [in real network systems, there may be different species of nodes with each species having different properties (*e.g.*, each species may have different probabilities for adding new nodes and may also have different attachment probabilities to the same node species and to other node species, etc.)]. (ii) initial link distributions [*i.e.*, when a new node is born, its number of links to old nodes is not necessarily a constant number, but, rather, is characterized by a given probability distribution p_k of new links].

As an application of our model, we investigate the movie-actor network with movies considered as nodes and actors as links (*i.e.*, if the same actor appears in two movies there is a link between the two movies [30]). Moreover, we consider theatrical movies and made-for-television movies to constitute two different species.

4.2 Growing Network Model

We construct a growing network model which incorporates multiple species and initial link probabilities. Given an initial network, we create new nodes at a constant rate. We let the new node belong to species j with probability $Q^{(j)}$ ($\sum_j Q^{(j)} = 1$). We decide how many links l the new node establishes with already existing nodes by randomly choosing l from a probability distribution $p_l^{(j)}$. Then, we randomly attach the new node to l existing nodes with preferential attachment probability proportional to a factor $A_k^{(j,i)}$, where k is the number of links of the target node of

species i to which the new node of species j may connect. That is, the connection probability between an existing node and a new node is determined by the number of links of the existing node and the species of the new node and the target node.

As for the single species case [25], the evolution of this model can be described by rate equations. In our case the rate equations give the evolution of $N_k^{(i)}$, the number of species i nodes that have k links,

$$\begin{aligned}\frac{dN_k^{(i)}}{dt} &= \sum_{j=1}^{S} Q^{(j)}\bar{k}^{(j)}\frac{\left[A_{k-1}^{(j,i)}N_{k-1}^{(i)} - A_k^{(j,i)}N_k^{(i)}\right]}{\sum_m\sum_k A_k^{(j,m)}N_k^{(m)}} \\ &\quad + Q^{(i)}p_k^{(i)}, \end{aligned} \tag{4.1}$$

where S is the total number of species and $\bar{k}^{(j)} = \sum_l l p_l^{(j)}$ is the average number of new links to a new node of species j, and t is normalized so that the rate of creation of new nodes is one per unit time. The term proportional to $A_{k-1}^{(j,i)}N_{k-1}^{(i)}$ accounts for the increase of $N_k^{(i)}$ due to the addition of a new node of species j that links to a species i node with $k-1$ connections. The term proportional to $A_k^{(j,i)}N_k^{(i)}$ accounts for the decrease of $N_k^{(i)}$ due to linking of a new species j node with an existing species i node with k connections. The denominator, $\sum_m\sum_k A_k^{(j,m)}N_k^{(m)}$, is a normalization factor. If we add a new node with l initial links, we have l chances of increasing/decreasing $N_k^{(i)}$. This is accounted for by the factor $\bar{k}^{(j)} = \sum_l l p_l^{(j)}$ appearing in the summand of Eq. (4.1). The last term, $Q^{(i)}p_k^{(i)}$, accounts for the introduction of new nodes of species i. Since all nodes have at least one link, $N_0^{(i)} = 0$.

4.3 Analysis of the Model

Equation (4.1) implies that total number of nodes and total number of links increase at fixed rates. The total number of nodes of species i increases at the rate

$Q^{(i)}$. Thus

$$\sum_k N_k^{(i)} = Q^{(i)} t. \tag{4.2}$$

The link summation over all species $\sum_i \sum_k k N_k^{(i)}$ is twice the total number of links in the network. Thus

$$\sum_i^S \sum_k k N_k^{(i)} = 2 \left\langle \dot{k} \right\rangle t, \tag{4.3}$$

where $\left\langle \dot{k} \right\rangle = \sum_i \sum_k Q^{(i)} k p_k^{(i)} = \sum_i Q^{(i)} \bar{k}^{(i)}$. Solutions of (4.1) occur in the form(*c.f.*, [25] for the case of single species nodes),

$$N_k^{(i)} = n_k^{(i)} t, \tag{4.4}$$

where $n_k^{(i)}$ is independent of t. Eq. (4.1) yields

$$n_k^{(i)} = \frac{B_{k-1}^{(i)} n_{k-1}^{(i)} + Q^{(i)} p_k^{(i)}}{(B_k^{(i)} + 1)}, \tag{4.5}$$

where $B_k^{(i)}$ is

$$B_k^{(i)} = \sum_{j=1}^S Q^{(j)} \bar{k}^{(j)} \frac{A_k^{(j,i)}}{\sum_m \sum_k A_k^{(j,m)} n_k^{(m)}}. \tag{4.6}$$

To most simply illustrate the effect of spread in the initial number of links, we first consider the case of a network with a single species of node and with a simple form for the attachment $A_k = A_k^{(1,1)}$. In particular, we choose [25], $A_k = k + c$. (Note that by Eq. (4.1) this is equivalent to $A_k = ak + b$ with $c = b/a$.) Inserting this A_k into Eq. (4.6), we obtain $\sum_k (k + c) n_k = 2\left\langle \dot{k} \right\rangle + cQ$ and $B_k = (k + c)/\eta$, where $\eta = (2\left\langle \dot{k} \right\rangle + cQ)/(Q\bar{k}) = 2 + c/\bar{k} \geq 2$. (Note that $\left\langle \dot{k} \right\rangle = Q\bar{k}$ for the single species case.) Thus Eq. (4.5) yields

$$[(k + c) n_k - (k + c - 1) n_{k-1}] + \eta n_k = \eta Q p_k. \tag{4.7}$$

Setting $p_k = p_1 (k + c)^{-\beta}$, we can solve Eq. (4.7) for large k by approximating the discrete variable k as continuous, so that

$$(k + c) n_k - (k + c - 1) n_{k-1} \cong \frac{d}{dk} [(k + c) n_k]. \tag{4.8}$$

Solution of the resulting differential equation,

$$\frac{d}{dk}[(k+c)n_k] + \eta n_k = \eta Q p_1 (k+c)^{-\beta}, \tag{4.9}$$

for n_k with $\beta \neq \eta+1$ consists of a homogeneous solution proportional to $(k+c)^{-(\eta+1)}$ plus the particular solution, $[\eta Q p_1/(\eta+1-\beta)](k+c)^{-\beta}$. For $\beta = \eta+1$ the solution is $n_k = \eta Q p_1 (k+c)^{-(\eta+1)} \ln[d(k+c)]$, where d is an arbitrary constant. Hence, for *sufficiently large* k we have $n_k \sim k^{-(\eta+1)}$ if $\beta > \eta+1$, and $n_k \sim k^{-\beta}$ if $\beta < \eta+1$. Thus the result for $\beta > \eta+1$ is independent of β and, for $c = 0$, coincides with that give in Ref. [24] ($\eta + 1 = 3$ when $c = 0$). Solutions of Eq. (4.7) for n_k versus k in the range $1 \leq k \leq 10^4$ are shown as open circles in Fig. 4.1(a) for initial link probabilities of the form

$$p_k = \begin{cases} p_1 k^{-1} & \text{for } 1 \leq k \leq 10^2 \\ p_1 10^{2(\bar{\beta}-1)} k^{-\bar{\beta}} & \text{for } k \geq 10^2, \end{cases} \tag{4.10}$$

which are plotted as solid lines in Fig. 4.1(a). The values of $\bar{\beta}$ used for the figure are $\bar{\beta} = 0.5, 1, 2, 3, 4$, and ∞ ($\bar{\beta} = \infty$ corresponds to $p_k \equiv 0$ for $k > 10^2$). For clarity n_k has been shifted by a constant factor so that n_1 coincides with the corresponding value of p_1. Also, to separate the graphs for easier visual inspection, the value of p_1 for successive $\bar{\beta}$ values is changed by a constant factor [since (4.7) is linear, the form of the solution is not effected]. We note from Fig. 4.1(a) that n_k follows p_k for $k < 10^2$ in all cases. This is as expected, since p_k decreases slower than k^{-3} in this range. Furthermore, n_k very closely follows p_k for $k > 10^2$ for $\bar{\beta} = 0.5, 1.0, 2.0$. As $\bar{\beta}$ increases deviations of n_k from p_k in $k > 10^2$ become more evident, and the large k asymptotic k^{-3} dependence is observed. Thus, if p_k decreases sufficiently rapidly, then the behavior of n_k is determined by the growing network dynamics, while, if p_k decreases slowly, then the behavior of n_k is determined by p_k.

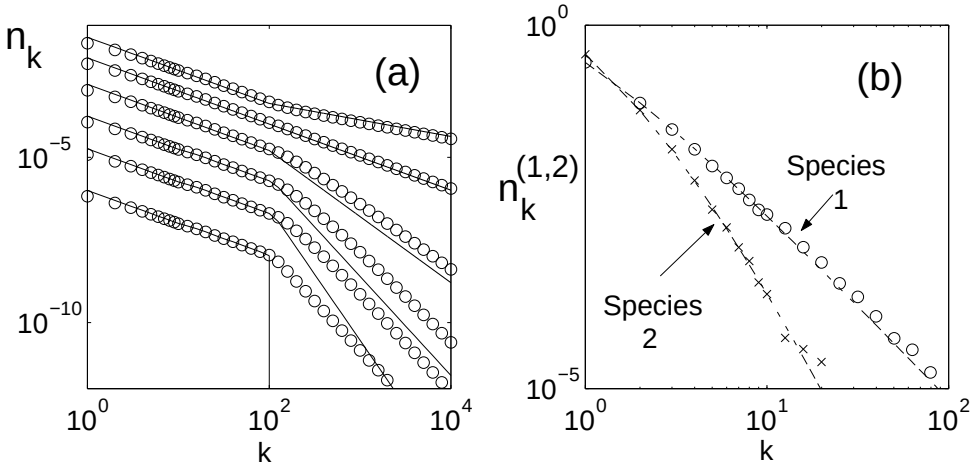

Figure 4.1: (a) n_k and p_k versus k for the single species network model. Solid lines are the initial link probability p_k and circles are the n_k obtained from Eq. (4.7). (b) $n_k^{(1)}$ and $n_k^{(2)}$ versus k for the two species network model. Circles (species 1) and crosses (species 2) are log-binned data from our numerical simulation. The total number of nodes in our numerical network system is 10^6. The dashed lines are solutions obtained from (4.5) and (4.13).

To simply illustrate the effect of multiple species we now consider a growing two species network with $p_k = \delta_{1,k}$ (*i.e.*, $p_k = 0$ for $k \geq 2$). Then, Eq. (4.6) becomes

$$B_k^{(1)} = \frac{Q^{(1)} A_k^{(1,1)}}{\sum_m \sum_k A_k^{(1,m)} n_k^{(m)}} + \frac{Q^{(2)} A_k^{(2,1)}}{\sum_m \sum_k A_k^{(2,m)} n_k^{(m)}}, \tag{4.11a}$$

$$B_k^{(2)} = \frac{Q^{(1)} A_k^{(1,2)}}{\sum_m \sum_k A_k^{(1,m)} n_k^{(m)}} + \frac{Q^{(2)} A_k^{(2,2)}}{\sum_m \sum_k A_k^{(2,m)} n_k^{(m)}}, \tag{4.11b}$$

where $\sum_m$ represents summation of species 1 and 2 nodes.

In order to illustrate the model with our numerical simulations, we specialize to a specific case. We choose attachment coefficients $A_k^{(1,1)} = ak$, $A_k^{(1,2)} = ak$,

$A_k^{(2,1)} = bk$, and $A^{(2,2)} = 0$. Thus a new species 1 node connects to either existing species 1 nodes and species 2 nodes with equal probability, while a new species 2 node can connect to existing species 1 nodes only. Therefore, the first summation term in Eq. (4.11), $\sum_m \sum_k A_k^{(1,m)} n_k^{(m)}$, becomes $a \sum_k (kn_k^{(1)} + kn_k^{(2)})$, which is a times the total increase of links at each time $a \times 2(Q^{(1)} + Q^{(2)})$. Recall that $Q^{(1)} + Q^{(2)} = 1$. In order to calculate the second summation term in Eq. (4.11), $\sum_m \sum_k A_k^{(2,m)} n_k^{(m)} = b \sum_k kn_k^{(1)}$, we define a parameter γ that is the ratio of the total number of links of species 1 to the total number of links in the network. Since the probability of linking a new species 1 node to existing species 1 nodes is determined by the total number of links of species 1, this probability is exactly same as γ. Thus, if we add a new species 1 node, the number of links of species 1 increases by $Q^{(1)}$ due to the new node and by $\gamma Q^{(1)}$ due to the existing species 1 nodes that become connected with the new node, while the number of links of species 2 increases by $(1-\gamma)Q^{(1)}$. But, if we add a new species 2 node, the numbers of links increases by $Q^{(2)}$ for both species because a new species 2 node can link to species 1 nodes only. Thus, the increase of species 1 links is $(1+\gamma)Q^{(1)} + Q^{(2)}$ and that of species 2 links is $(1-\gamma)Q^{(1)} + Q^{(2)}$. Since γ is the ratio of the number of species 1 links to the total number of links, $\gamma = [(1+\gamma)Q^{(1)} + Q^{(2)}]/2$ or

$$\gamma = \frac{1}{2 - Q^{(1)}}. \tag{4.12}$$

With this γ, Eq. (4.11) becomes

$$B_k^{(1)} = \frac{Q^{(1)}}{2} k + \frac{Q^{(2)}(2 - Q^{(1)})}{2} k = \frac{k}{\eta^{(1)}}, \tag{4.13a}$$

$$B_k^{(2)} = \frac{Q^{(1)}}{2} k = \frac{k}{\eta^{(2)}}. \tag{4.13b}$$

where obtain $\eta^{(1)} = 2/[Q^{(1)} + Q^{(2)}(2 - Q^{(1)})]$ and $\eta^{(2)} = 2/Q^{(1)}$.

Proceeding as for the single species case, we approximate (4.5) by an ordinary differential equation (*c.f.*, Eq. (4.9)) to obtain $n_k^{(i)} \sim k^{-(1+\eta^{(i)})}$. As an example, we set $Q^{(1)} = Q^{(2)} = 0.5$, in which case Eqs. (4.13) give exponents $1 + \eta^{(1)} = 2.6$ and $1 + \eta^{(2)} = 5$. In Fig. 4.1(b) we plot, for this case, the analytic solution obtained from (4.5) and (4.13) as dashed lines, and the results of numerical simulations as open circles and pluses. The simulation results, obtained by histogram binning with uniform bin size in $\log k$, agree with the analytic solutions, and both show the expected large k power law behaviors, $n_k^{(1)} \sim k^{-2.6}$ and $n_k^{(2)} \sim k^{-5}$.

4.4 The Movie-Actor Network

We now investigate the movie-actor network. We collected data from the Internet Movie Data Base (IMDB) web site [31]. The total number of movies is 285,297 and the total number of actors/actresses is 555,907. Within this database are 226,325 theatrical movies and 24,865 made for television movies. The other movies in the database are made for television series, video, mini series, and video games. In order to get good statistics, we choose only theatrical and television movies made between 1950 to 2000. Thus we have two species of movies. We also consider only actors/actresses from these movies. We consider two movies to be linked if they have an actor/actress in common [32]. We label the theatrical movies species 1, and the made for television movies species 2.

In order to apply our model, Eq. (4.1), we require as input $Q^{(j)}, p_k^{(j)}$ and $A_k^{(j,i)}$ which we obtain from the movie-actor network data. For simplicity, we assume these quantities to be time-independent [33]. We take $Q^{(1)}$ and $Q^{(2)}$ to be, respectively, the fractions of theatrical and made for television movies in our data base. We obtain $Q^{(1)} = 0.83$ and $Q^{(2)} = 0.17$. We now consider $p_k^{(j)}$. Suppose

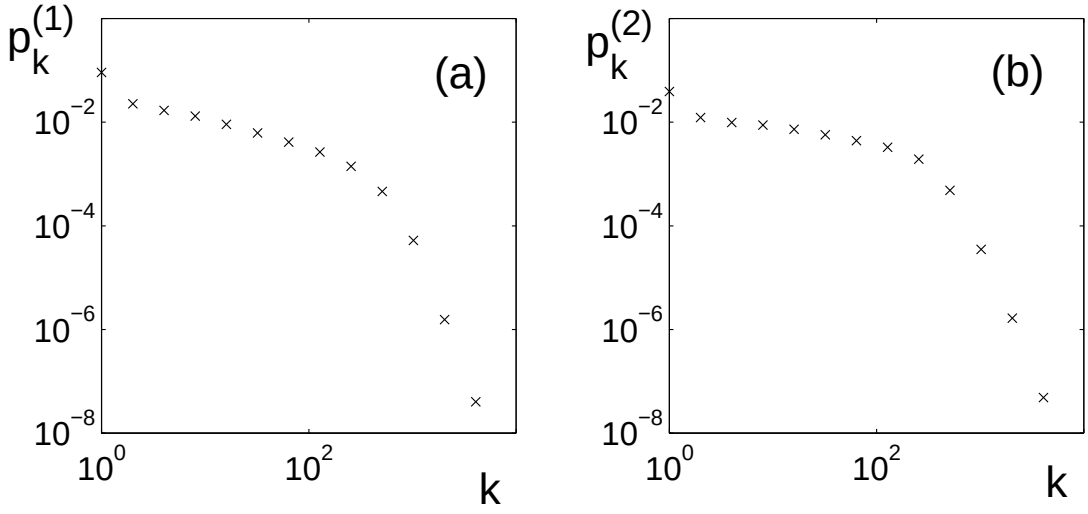

Figure 4.2: The initial link probability distributions p_k of (a) theatrical movies and (b) television movies. These plots are obtained using bins of equal width in $\log k$ and dividing the number of nodes in each bin by the product of the bin width in k (which varies from bin to bin) and the total number of nodes.

a new movie is produced casting r actors. For each actor s ($s = 1, 2, ..., r$) let l_s denote the number of previous movies in which that actor appeared. Then the total number of the initial links of the new movie is $\sum_s l_s$. From histograms of this number, we obtain (Figs. 4.2) the initial link probability distributions $p_k^{(j)}$.

The attachment $A_k^{(j,i)}$ can be numerically obtained from data via,

$$A_k^{(j,i)} \sim \frac{\langle \Delta(j;i,k) \rangle}{\delta t}, \tag{4.14}$$

where $\Delta(j;i,k)$ is the increase during a time interval δt in the number of links between old species i nodes that had k links and new species j nodes, and $< ... >$ is an average over all such species i nodes [34]. In the movie network, we count all movies and links from 1950 to 1999, and measure the increments in the number of links for a δt of one year. We obtain attachment coefficient $A_k^{(1,1)} \sim 0.10k^{0.59}$

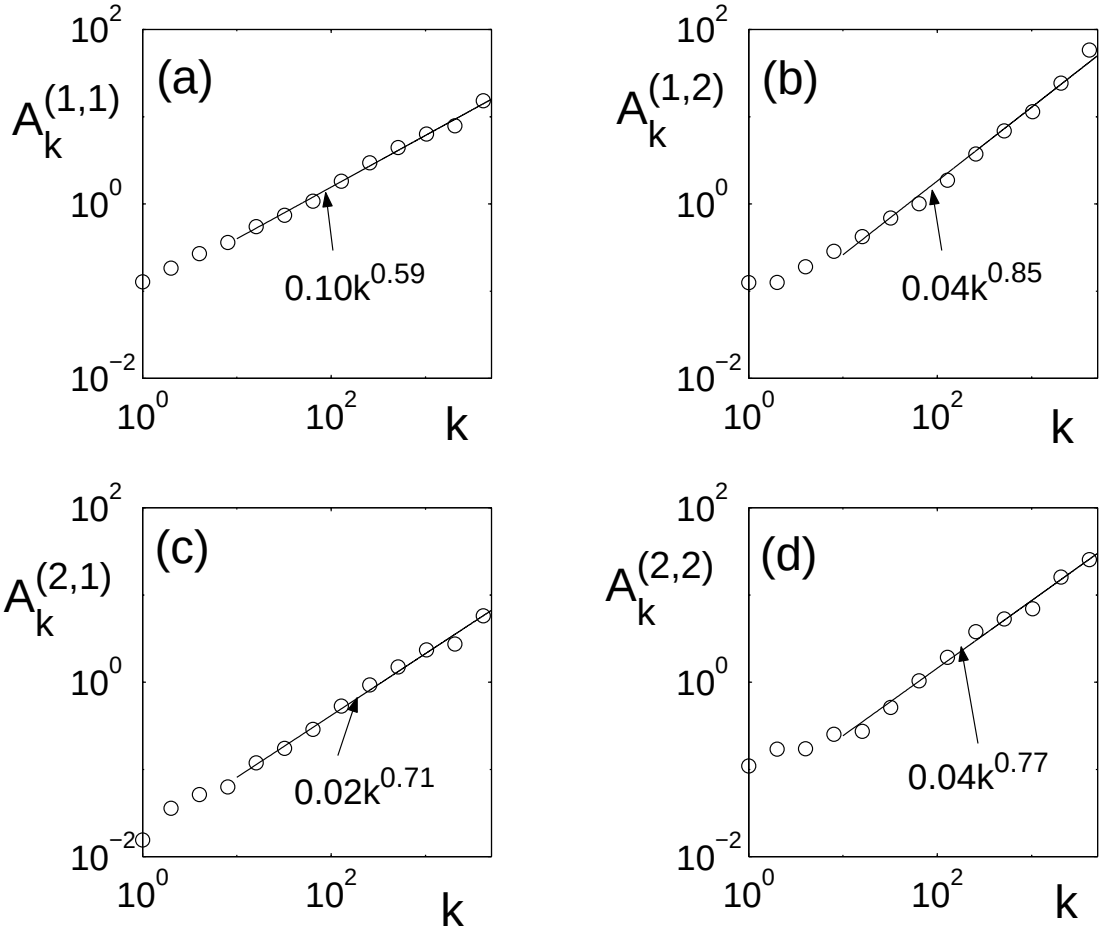

Figure 4.3: Attachment coefficients for theatrical movies (a) $A_k^{(1,1)}$ and (b) $A_k^{(1,2)}$, and for television movies (c) $A_k^{(2,1)}$ and (d) $A_k^{(2,2)}$. All data are obtained using log-binning without normalization (see caption to Fig. 4.2).

and $A_k^{(1,2)} \sim 0.04k^{0.85}$ for theatrical movies, and $A_k^{(2,1)}0 \sim 0.02k^{0.71}$ and $A_k^{(2,2)} \sim 0.04k^{0.77}$ for television movies. See Fig. 4.3.

Incorporating these results for $Q^{(i)}$, $p_k^{(i)}$ and $A_k^{(j,i)}$ in our multi-species model, Eq. (4.1), we carry out numerical simulations as follows: (i) We add a new movie at each time step. We randomly designate each new movie as a theatrical movie with probability $Q^{(1)} = 0.83$ or a television movie with probability $Q^{(2)} = 0.17$. (ii)

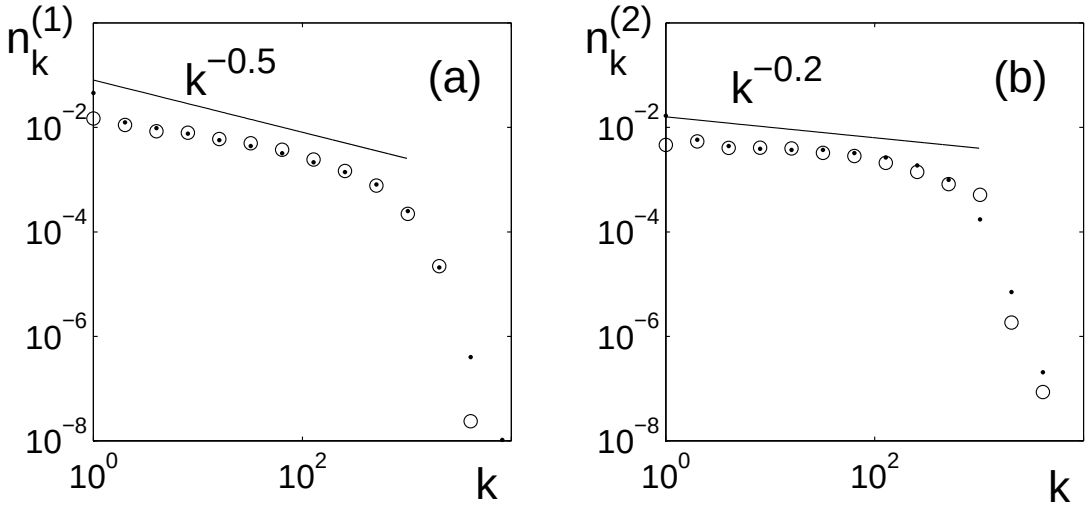

Figure 4.4: The probability distributions $n_k^{(i)}$ of movies that have k links; (a) theatrical movies $n_k^{(1)}$ and (b) television movies $n_k^{(2)}$. Dots are $n_k^{(i)}$ obtained from the movie network while circles are from numerical simulation using $Q^{(j)}$ obtained from our data base, $p_k^{(j)}$ in Fig. 4.2 and $A_k^{(j,i)}$ in Fig. 4.3. All data are obtained using log-binning (see caption to Fig. 4.2).

With initial link probability $p_k^{(j)}$, we randomly choose the number of connections to make to old movies. (iii) We then use the attachment $A_k^{(j,i)}$ to randomly choose connections of new species j movie to old species i movies. (iv) We repeat (i)-(iii) adding 100,000 new movies, and finally calculate the probability distributions of movies with k links.

Figure 4.4 shows $n_k^{(i)}$ versus k obtained from our movie-actor network data base (dots) and from numerical simulations using Eq.(4.1) (open circles) with our empirically obtained results for $Q^{(j)}$, $p_k^{(j)}$, and $A_k^{(j,i)}$. The results are roughly consistent with the existence of two scaling regions [35]. For small k ($k \lesssim 10^2$) the two species exhibit slow power law decay with different exponents, $n_k^{(1)} \sim k^{-0.5}$,

$n_k^{(2)} \sim k^{-0.2}$, while for large k the probabilities decay much more rapidly. Indeed, the results of [25] suggest that the decay should be exponential for large k since the attachment $A_k^{(j,i)}$ grow sub-linearly with k. We showed in Sec. 4.3 for the single species model with a linear attachment $A_k \sim k$ that n_k follows p_k when p_k decays slowly, while n_k is independent of p_k when p_k decays sufficiently quickly. As we will later show, this feature is also applicable to multi-species networks with nonlinear attachments. As seen in Figs. 4.5(a) and 4.5(b), $n_k^{(i)}$ follows $p_k^{(i)}$ in the small k region. However, it is not clear whether $n_k^{(i)}$ follows $p_k^{(i)}$ in the large k region. In order to check the behavior of $n_k^{(i)}$ in this region, we carried out another numerical simulation using an initial link probability $\bar{p}_k^{(i)}$ which is cut off at $k = 50$. That is, $\bar{p}_k^{(i)} = p_k^{(i)} / \sum \bar{p}_k^{(i)}$ when $k \leq 50$ and $\bar{p}_k^{(i)} = 0$ when $k > 50$. Using $\bar{p}_k^{(i)}$ in place of $p_k^{(i)}$, we obtain from our simulation corresponding data, $\bar{n}_k^{(i)}$ versus k, which are shown in Figs. 4.5(c) and 4.5(d) as filled in circles. For comparison the data for $n_k^{(i)}$ from Figs. 4.5(a) and 4.5(b) are plotted in Figs. 4.5(c) and 4.5(d) as open circles. It is seen that the cutoff at $k = 50$ induces a substantial change in the distribution of the number of links for $k > 50$. Thus it appears that, in the range tested, the large k behavior of the movie-actor network is determined by the initial link probability $p_k^{(i)}$ rather than by the dynamics of the growing network.

4.5 Summary

In this chapter we propose a model for the evolution of the distribution $n_k^{(i)}$ of links k per node of i species: a growing multi-species network with variable initial link probabilities $p_k^{(i)}$. We have analyzed our model in two extreme cases. In the case of a network with a single species of nodes, we found that the behavior of n_k is determined by the growing network dynamics if p_k decreases sufficiently

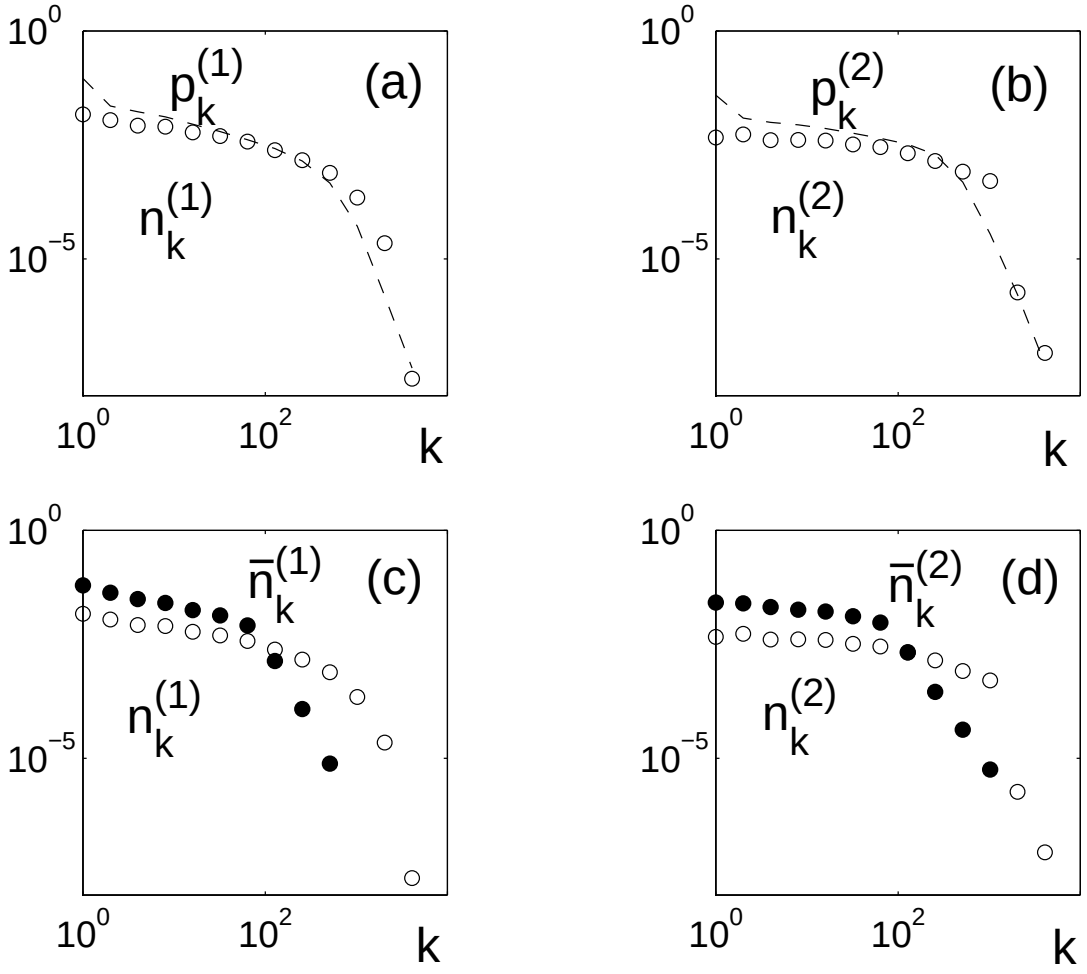

Figure 4.5: (a) and (b) are $n_k^{(i)}$ (circles) obtained from numerical simulations using $p_k^{(i)}$ (dashed lines), while (c) and (d) show $n_k^{(i)}$ from (a) and (b) (open circles) plotted with results denoted $\bar{n}_k^{(i)}$ (filled circles) from simulation using a cutoff initial link probability $\bar{p}_k^{(i)}$ (where $\bar{p}_k^{(i)} = p_k^{(i)} / \sum \bar{p}_k^{(i)}$ when $k \leq 50$ and $\bar{p}_k^{(i)} = 0$ when $k > 50$). All data are obtained using log-binning (see caption to Fig. 4.2).

rapidly, while the behavior of n_k is determined by p_k if p_k decreases slowly. In the case of a network with two species of nodes with $p_k = \delta_{1,k}$, we found that the attachment coefficients determine the behavior of $n_k^{(i)}$. In particular, each species

may show different power law behaviors. We have also investigated the movie-actor network as an example. We believe that the effect of multiple species nodes may be important for modeling other complicated networks (*e.g.*, the world wide web can be divided into commercial sites and educational or personal sites). We also conjecture that the initial link probability is a key feature of many growing networks.

BIBLIOGRAPHY

[1] W. Losert, D. G. W. Cooper, and J. P. Gollub, Phys. Rev. E **59**, 5855 (1999).

[2] I. V. Melnikov, D. A. Egolf, S. Jeanjean, B. B. Plapp, and E. Bodenschatz, in *Stochastic Dynamics and Pattern Formation in Biological and Complex Systems,* edited by S. Kim, K. J. Lee, T. K. Lim, and W. Sung, AIP Conf. Proc. 501 (AIP, Woodbury, NY, 2000), p. 36.

[3] S. C. Venkataramani, and E. Ott, Phys. Rev. Lett. **80**, 3495 (1998).

[4] A.-L. Barabási and H. E. Stanley, *Fractal Concepts in Surface Growth* (Cambridge University Press, Cambridge, 1995).

[5] This general viewpoint was also adopted in Ref. [3] where, motivated by experimentally observed phenomena [F. Melo, P. B. Umbanhowar, and H. L. Swinney, Phys. Rev. Lett. **75** , 3838 (1995)], other choices for M and f were employed. In that case the objective was to check the hypothesis that period doubling in conjunction with pattern formation at a preferred scale were the essential ingredients necessary to explain the observed bifurcations and the evolution of time periodic patterns occurring in a vertically oscillated granular layer of the order of 10 grains thick.

[6] M. Kardar, G. Parisi, and Y. C. Zhang, Phys. Rev. Lett. **56**, 889 (1986).

[7] Cusp formation also occurs for the Kardar-Parisi-Zhang equation; see Fig. 1 of Ref. [6].

[8] A. R. Osborne, M. Onorato, and M. Serio, Phys. Lett. A **275** , 386(2000).

[9] E. J. Boettcher, J. Fineberg, and D.P. Lathrop, Phys. Rev. Lett. **85** 2030(2000).

[10] M. Bartuccelli, *et al.*, Physica D **44** , 421(1990). They draw a phase diagram figures for NLS equation (Fig. 1) and CGL equation (Fig. 2).

[11] C. D. Levermore and M. Oliver, Lect. Appl. Math. **31** 141(1996).

[12] Y. Kuramoto, *Chemical Oscillations, Waves and Turbulence* , Series in Synergetics **19** , Springer, New York, 1984.

[13] K. Stewartson and J.T. Stuart, J. Fluid Mech. **48** , 529(1971).

[14] A.C. Newell and J.A. Whitehead, J. Fluid Mech. **38** , 279(1969).

[15] G. Ahlers and D.S. Cannell, Phys. Rev. Lett. **50** , 1583(1983).

[16] H.-K. Park, Phys. Rev. Lett. **86** 1130(2000); also see the references therein.

[17] $P(|A|)$ is to be contrasted with the probability distribution of a single burst amplitude $P_h(|A|)$ to be discussed in Sec. 3.4.

[18] P. Coullet, Phys. Rev. Lett **56** , 724(1986).

[19] C. Elphick, A. Hagberg, and E. Meron, Phys. Rev. Lett **80** , 5007(1998).

[20] G. Fibich and D. Levy, Phys. Lett. A **249** , 286(1998).

[21] B. LeMesurier, *et al.*, Physica D **32** , 210(1988).

[22] H. Iwasaki and S. Toh, Prog. Theo. Phys. **87**, 1127 (1992).

[23] S.N. Dorogovtsev and J.F.F. Mendes, ArXiv:cond-mat/0106144 v1 7 Jun 2001. They summarize values of γ for several network systems in Table I.

[24] A.-L. Barabási and R. Albert, Science **286**, 509(1999).

[25] P.L. Krapivsky and S. Redner, Phys. Rev. E 6306(6):6123 (2001); See also P.L. Krapivsky, S. Render, and F. Leyvraz, Phys. Rev. Lett. **85**, 4629(2000).

[26] S.N. Dorogovtsev, J.F.F. Mendes, and A.N. Samukhin Phys. Rev. Lett. **85**, 4633(2000).

[27] S.N. Dorogovtsev and J.F.F. Mendes, Phys. Rev. E **62**, 1842(2000).

[28] R. Albert and A.-L. Barabási, Phys. Rev. Lett. **85**, 5234(2000).

[29] S.H. Yook, H. Jeong, and A.-L. Barabási, Phys. Rev. Lett. **86**, 5835(2001).

[30] Barabási and Albert also investigated the movie-actor network. However, they consider actors as nodes that are linked if they are cast in the same movie. See Ref. [24] and Ref. [28].

[31] The Internet Movie Database, http://www.imdb.com

[32] This scenario could be more accurately modeled by tracking the connectivity of actors/actresses as well as movies. In particular, actors/actresses who appear in many movies cause correlations between movie links that are not present in our model.

[33] The a priori degree distribution of the movie network is time dependent since it depends on the personal history of all actors. In a more complete growth dynamics this fact should be taken into account.

[34] The technique we use for obtaining $A_k^{(j,i)}$ is similar to that used by H. Jeong *et al.* who presume single species situations (in which case the superscripts j, i do not apply). [H. Jeong, Z. Néda, and A.-L. Barabási, ArXiv:cond-mat/0104131 v1 7 Apr 2001.]

[35] Similar observations suggesting two scaling regions have also been recently observed in other cases of growing networks. Barabási *et al.* investigated the scientific collaboration network [A.-L. Barabási, *et al.*, ArXiv:cond-mat/0104162 v1 10 Apr 2001]. They argue that a model in which links are continuously created between existing nodes explains the existence of two scaling regions in their data. Vazquez investigated the citation network of papers (nodes) and authors (links) for Phys. Rev. D and found two scalings in its in-degree distribution. See A. Vazquez, ArXiv:cond-mat/0105031 v1 2 May 2001.